IOPscience iopscience.iop.org

Home Search Collections Journals About Contact us My IOPscience

Self-assembly of InAs and Si/Ge quantum dots on structured surfaces

This article has been downloaded from IOPscience. Please scroll down to see the full text article.

2004 J. Phys.: Condens. Matter 16 S1503

(http://iopscience.iop.org/0953-8984/16/17/005)

View the table of contents for this issue, or go to the journal homepage for more

Download details:
IP Address: 129.252.86.83
The article was downloaded on 27/05/2010 at 14:29

Please note that terms and conditions apply.

INSTITUTE OF PHYSICS PUBLISHING JOURNAL OF PHYSICS: CONDENSED MATTER

J. Phys.: Condens. Matter **16** (2004) S1503–S1534 PII: S0953-8984(04)66822-6

Self-assembly of InAs and Si/Ge quantum dots on structured surfaces

F Patella[1], A Sgarlata[1], F Arciprete[1], S Nufris[1], P D Szkutnik[1], E Placidi[1], M Fanfoni[1], N Motta[2] and A Balzarotti[1]

[1] Dipartimento di Fisica, Università di Roma 'Tor Vergata' and Istituto Nazionale per la Fisica della Materia, Via della Ricerca Scientifica, 1-00133 Roma (I), Italy
[2] Dipartimento di Fisica, Università di Roma Tre and Istituto Nazionale per la Fisica della Materia, Via della Vasca Navale 84, 00146 Roma (I), Italy

E-mail: patella@roma2.infn.it

Received 30 July 2003
Published 16 April 2004
Online at stacks.iop.org/JPhysCM/16/S1503
DOI: 10.1088/0953-8984/16/17/005

Abstract
We discuss the self-aggregation process of InAs and Si–Ge quantum dots (QDs) on natural and patterned GaAs(001) and Si(001) and Si(111) surfaces, with reference to our recent studies with scanning tunnelling and atomic force microscopy and current experimental and theoretical works. Various methods for obtaining naturally structured surfaces are briefly surveyed, as the patterning formed by the surface instability and by the strain in mismatched heteroepitaxy, and the latest methods of pre-patterning and growth at selected sites are discussed. Basic topics are also addressed that determine the final morphology of QDs, such as the wetting layer formation, the elastic strain field and the two-dimensional to three-dimensional phase transition.

(Some figures in this article are in colour only in the electronic version)

1. Introduction

New frontiers in nanodevice technology based on III–V and IV–IV semiconductor quantum dots (QDs) require the fabrication of epitaxial structures with atomic-scale control of the single aggregate. Promising applications, currently under test, span from nanomemories to single emitters, single-electron devices and quantum cellular automata. Most of them rely on the possibility of precisely positioning the nucleation site on the surface and controlling the shape and size of the dots.

Among methods of fabrication for ordered arrays of nanostructures, growth on substrates pre-patterned by conventional e-beam lithography (EBL) retains wide relevance because of its versatility. However, the coherence of the crystalline islands and the reduced number of

 © 2004 IOP Publishing Ltd Printed in the UK

defects achieved in the epitaxial self-assembly process make techniques such as molecular beam epitaxy (MBE), chemical vapour deposition (CVD), physical vapour deposition (PVD) and metal organic vapour phase epitaxy (MOVPE) appealing alternatives to e-beam patterning, provided that their limitations in the control of lateral position and size of islands are overcome. The target of overcoming these limitations has focused new attention on the basic mechanisms and microscopic processes of epitaxial growth, particularly of MBE, in the attempt to order QDs on naturally patterned substrates such as vicinal and high-index surfaces. At the same time, artificial means of surface nanostructuring, diverse from EBL, have been developed by using probes with a high spatial resolution, such as scanning tunnelling microscopy (STM) and focused ion beam (FIB) techniques.

STM and atomic force microscopy (AFM) are the most suitable tools for investigating the properties of these structures, and many results shown in this paper involve these techniques. Microscopic-size scanning probes are also used to artificially nanostructure the surface to create small pits which act as nucleation centres and/or to locally oxidize the substrate.

This paper mainly reports on our results on two systems of wide technological interest, i.e. InAs/GaAs and Si–Ge/Si; both can be considered prototypes for experimental and theoretical studies of a broad class of heterostructures with high and low mismatch, respectively.

In the following sections we first describe the macroscopic and microscopic structure of real surfaces and their evolution in the model cases of GaAs(001) and Si(001) and Si(111), with reference to theoretical models that consider thermodynamic and kinetic instabilities inherent in the growth process. Then we discuss different methods of obtaining nanostructured surfaces; in particular, the natural patterning formed by the instability of the surface, and other artificial means of guiding adatom nucleation based on substrate pre-patterning and subsequent island growth at selected surface positions. Three such techniques, STM, FIB and EBL, will be addressed here. Other issues that are basic in determining the final morphology of the QD ensemble, such as the formation of a wetting layer (WL), the elastic strain field, the two-dimensional (2D) to three-dimensional (3D) transition and finally the 3D structures and their lateral ordering, are discussed throughout the paper. The reference made to the huge existing literature on these topics cannot be but incomplete.

2. Experimental techniques and sample preparation

The InAs/GaAs samples investigated in this work were grown by conventional solid source MBE equipped with reflection high-energy electron diffraction (RHEED) for *in situ* monitoring of the growth. The typical procedure is as follows. Prior to InAs deposition, a GaAs buffer of approximately 0.75 μm is grown on the (001) oriented substrate, in As_4 overflow, at 590 °C and at a rate of 1 μm h^{-1}. After 10 min post-growth annealing, the temperature is lowered to 500 °C for the InAs deposition. This determines the transition of the GaAs(001) surface reconstruction from (2×4) to c(4×4). The InAs is evaporated at a rate of 0.029 monolayers per second (ML s^{-1}) and the In delivery time is cycled in 5 s of evaporation followed by 25 s of growth interruption until the given thickness is reached. This procedure helps to equilibrate the surface at each deposition step by enhancing the migration of cation adatoms prior to incorporation into the lattice [1]. Together with the low growth rate this allows reduction of the kinetic factors hindering thermodynamic driving forces. Three multistacked structures consisting of five layers of InAs (about 2.7 ML each) intercalated by GaAs spacer layers of 20, 50 and 100 ML were prepared at 500 °C using the same growth parameters as for the single dot layer.

The 2D–3D transition is marked by a change of the RHEED pattern, along the [110] azimuth, from streaky to spotty. The onset of the transition is established at the edge of

the steep rise in the intensity of the RHEED signal. This onset is quite reproducible in the evaporation timescale and corresponds to the delivery of about 1.6 ML of InAs.

STM/AFM microscopy and low-energy electron diffraction (LEED) on InAs/GaAs systems is applied *ex situ* in ultrahigh vacuum (UHV). AFM images, acquired in the non-contact mode, are used to visualize the large-scale morphology of both the WL and the QDs.

Atomic scale details of the various samples are revealed by STM. In this case, to preserve the surface of the III–V materials during transport in air from the MBE to a UHV STM/AFM Omicron microscope, the growth terminates by deposition of a capping As layer of about 1 μm at a temperature of $-20\,^{\circ}$C. Subsequently, the cap is removed, by annealing in UHV at about 300 °C and the surface characterized by LEED. The desorption of the physisorbed As is monitored by a mass spectrometer, and care is taken not to overcome the activation temperature of the process. This procedure, which is commonly applied on III–V epitaxial surfaces, may introduce a small degree of local topological disorder but maintains the original reconstruction of the underlying surface [2]. For the strained InAs/GaAs phase, comparison with published *in situ* STM data [3] confirms this point.

The Si–Ge/Si studies are performed *in situ* in the STM/AFM chamber (base pressure below 4×10^{-9} Pa) equipped with different evaporation sources. Si(001) (p type, $\rho = 0.1$–$0.5\ \Omega$ cm) and (111) (n-type, $\rho = 10^{-3}\ \Omega$ cm, miscut angle $<0.5°$) substrates, are cleaned by Joule effect flashing the samples with dc current for 30–60 s at about 1250 °C. Germanium is deposited on Si-annealed substrates by PVD at low evaporation rates (about 3×10^{-4} ML s^{-1}). The geometrical arrangement of the STM system allows imaging *during* deposition at variable substrate temperatures [4]. Different movies have been acquired showing the evolution of the growth.

3. Instability of real surfaces and macroscopic roughening

Many physical situations in real surfaces lead to kinetic and/or thermodynamic instabilities of the growing front in the non-equilibrium epitaxy of a solid from its gas phase, as occurs in MBE and other epitaxial techniques. Though starting from low-index, high-symmetry substrates, the stochastic nature of the growth process brings about an intrinsic instability, which leads, for most semiconductors and metals, to the coarse-grained morphology of the terminating plane visible in the AFM and STM large-scale topographies.

Many factors can cause kinetic instabilities, such as anisotropy of the diffusion current induced by the surface reconstruction [5], the presence of impurities [6, 7], asymmetry in the rate of attachment at step edges [8], elasticity [9] and electromigration [10]. They produce macroscopic roughening that can give rise to step bunching, step-edge meandering on vicinal orientations and mounds on singular surfaces. Most of the time an increase in the substrate temperature can lower kinetic instabilities; however, in the epitaxy of mismatched heterostructures, it may also increase thermodynamic instabilities like the formation of misfit dislocations, ‘coherent’ isolated clusters, wavy deformation of the surface, etc [11].

The roughening of a growing surface is of very general theoretical interest in addition to the obvious technological relevance for materials based on GaAs and Si. Growth models predict asymptotic dynamical scaling behaviour of the roughness, which may increase in time according to power laws defining universality classes [12–14]. Theoretical approaches are essentially of two types: atomistic models based on first-principles calculations providing the energetic of atomic motions, and continuum models based on linear or non-linear equations, whose predictions are generally limited to the large-scale long-time macroscopic behaviour of the surface and to collective aspects of the growth. The most thoroughly studied continuum theory of kinetic roughening relies on the Kardar–Parisi–Zhang (KPZ)

non-conserving equation [15] that is a valid description of the behaviour of a moving interface whenever the velocity normal to the average surface has a non-linear component dependent on the local orientation. Since the seminal paper of KPZ, many other theories have been developed to model a large variety of growth processes. The validity of such linear and non-linear continuum theories applied to MBE growth is amply discussed in the literature (see [12–14] and references therein).

It is widely accepted that MBE depositions are often carried out at temperatures where growth could be considered a conservative process dominated solely by surface diffusion, and non-linear mechanisms such as desorption and defect formation can be disregarded. Instabilities of the KPZ type, therefore, do not occur in the majority of MBE growth processes.

Within the limit of an ideal conserving process, surface diffusion provides the mechanism for describing roughening and scaling properties of the growth at the coarse-grained length scale. The diffusion current **J**, driven by the gradient of the local chemical potential, must satisfy the continuity equation:

$$\partial h/\partial t = -\nabla \cdot \mathbf{J} + F, \tag{1}$$

where h is the surface height at a given point at time t, and F is the impinging flux inclusive of the stochastic noise. Since the growth equation cannot depend on the initial time or on the particular origin chosen on the surface for the description, it does not contain explicitly h and t but only linear and/or non-linear terms of ∇h describing the different processes involved. The equilibrium surface diffusion is accounted for by the linear term, $-K\nabla^4 h$, and the corresponding growth equation is stable. Yet in this case, instabilities may arise because of the non-equilibrium contribution to the diffusion current due to the stochastic nature of the impinging flux. In this case, the current itself may depend on the local curvature, i.e. $\mathbf{J} \propto \nabla h$, and a non-equilibrium term, $-|\upsilon|\nabla^2 h$, adds to the growth equation leading to instability [12, 13].

3.1. GaAs(001) surface

The experimental observations in many systems as, for instance, in GaAs(001) homoepitaxy, confirm the predictions of continuum theories for the asymptotic behaviour of the surface morphology. Growth on the singular (001) surface proceeds layer-by-layer with the initial nucleation of 2D islands that, on increasing deposition, coalesce in wide terraces. The step front of the terrace spreads out and meanders; meanwhile islands of the next layer start nucleating on top of the largest terraces. The AFM images of figure 1 show the morphology of two 0.75 μm GaAs epilayers grown on the (001) surface [16]. The homoepitaxy is performed at 590 °C (figure 1(a)) and at 500 °C (figure 1(b)) with an As/Ga flux ratio of 10; as a consequence, growth along the [001] direction proceeds through a surface plane having (2×4) reconstruction in the former case and c(4×4) in the latter. The corresponding height distributions of the surface profile, whose standard deviations σ are the surface roughnesses, are shown below the topographies. The values are close in the two cases, indicating a similar mechanism of growth. A few mounds (elongated bright structures in figure 1(a)) form on the (2×4) epilayer [17]; this is in qualitative agreement with both continuum theories [18] and simulations of thick-layer growth on high-symmetry surfaces [19], which envisage the break-up of step instabilities into pyramid-like features. The ripples are about 2.5 nm high (i.e. six to eight bilayers) and extend $\sim$0.8 μm in the $[1\bar{1}0]$ direction and $\sim$0.2 μm in the [110]. On the c(4×4) surface the ripples are fewer and smaller (about 1.5 nm high, i.e. four to five bilayers). These main topological characteristics, observed in many experiments [19–21], are rather independent of initial details of the real surface as, for instance, the presence of impurities or the step density due to miscut.

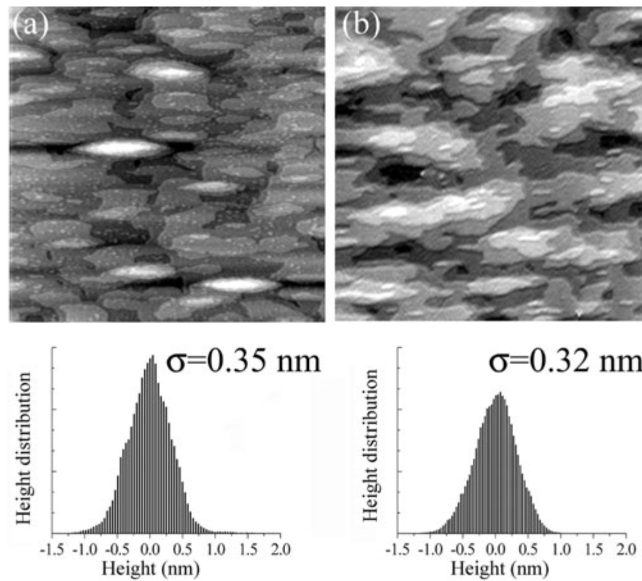

Figure 1. AFM topographies, (2.5×2.5) μm^2, of a 0.75 μm GaAs film grown on GaAs(001)(2×4) substrate at $T = 590\,^\circ$C (a), and on a GaAs(001)–c(4×4) substrate at $T = 500\,^\circ$C (b). The corresponding distributions of the surface height and the surface roughness, σ, are reported below.

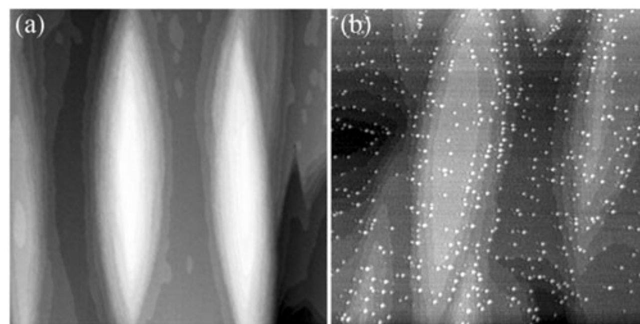

Figure 2. AFM images (1.5×1.5) μm^2 of InAs depositions on GaAs(001): (a) 1.1 ML, (b) 1.8 ML. A stepped surface with mounds elongated in the $[1\bar{1}0]$ direction is visible at subcritical depositions. At 1.8 ML, 3D QDs align along step edges.

In particular, we detect the same final morphology of the epilayer using GaAs(001) substrates with miscut between 0.25° and 0.01°, corresponding to initial average step distances between 100 and 2000 nm, respectively.

The morphology of the buffer layer plays an important role in the mismatched heteroepitaxy on which the self-aggregation process is based, for at least two main reasons. The first is that the buffer layer is the template for the pseudomorphic 2D growth of the WL, up to the critical thickness. The second is that the stepped texture of its surface fully determines the lateral order of the QD ensemble in the subsequent 2D–3D relaxation process. The AFM images of figure 2 illustrate these two effects by showing the stepped surface of the WL at subcritical depositions of InAs on GaAs(001) and the subsequent decoration of steps by QDs after the 2D–3D transition.

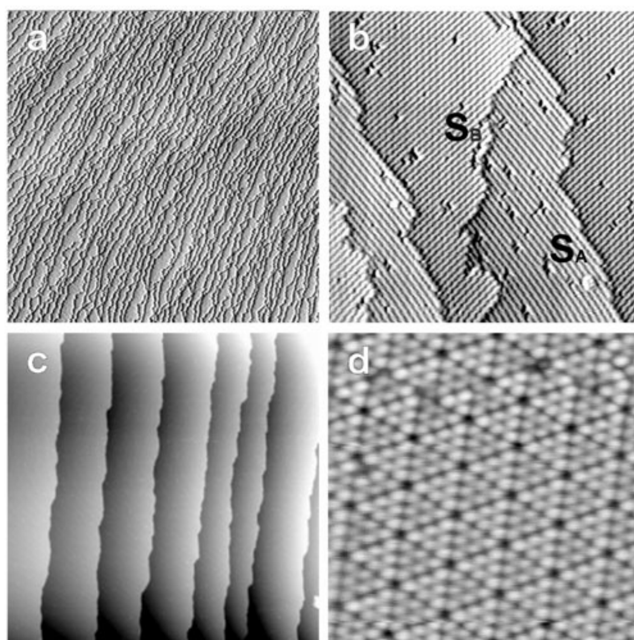

Figure 3. STM images of clean silicon surfaces: (a) Si(001) surface (3000×3000) nm^2. (b) High resolution image (50×50) nm^2. The two kind of steps, S_A and S_B, are indicated. (c) Si(111) surface (1000×1000) nm^2. (d) High-resolution image (15×15) nm^2 showing the 7×7 reconstruction.

3.2. Si(001) and (111) surfaces

The Si(001) 2×1 surface shows alternatively two kinds of steps, due to atom dimerization on perpendicular directions. According to Chadi [22], steps are classified as S_A or S_B, depending on the direction of the dimer rows with respect to the step edge. In the straight S_A steps, dimer rows on the upper terrace are parallel to the step edge, while dimer rows on terraces ended by roughened S_B step edges, are perpendicular (see figure 3). In both cases the step height is 0.136 nm.

Si(111) surfaces show steps fully (7×7) reconstructed with a height of 0.314 nm that corresponds to a bilayer [23]. The morphological properties of these steps, such as their width and density, depend on both the miscut angle and on the flashing procedures that can produce step bunching on a vicinal surface (see the next section). Two growth regimes, island nucleation or step-flow growth, are observed on these surfaces depending on the temperature of the substrate and on the Si flux [24, 25].

In figure 4, two sequences of four images, extracted from movies acquired at a sample temperature of 600 °C, show the homoepitaxial growth of Si on both (001) and (111) substrates. For Si on Si(001), the step-flow growth induces a change from a straight to a zig-zag edge for the steps, due to growth enhancement along the orthogonal direction (see figure 5). A different mechanism takes place in the case of Si(111) homoepitaxy. On terraces, Si atoms form small 2D islands that increase their size up to coalescence and formation of a complete new flat layer. Voigtländer [26] has extensively reviewed these topics.

4. Kinetic instability of real surfaces at mesoscopic scales

On a coarse-grained scale, the rippled morphology of the surface (figure 1) can be described in the frame of continuum theories; features such as step-edge meandering and/or step bunching,

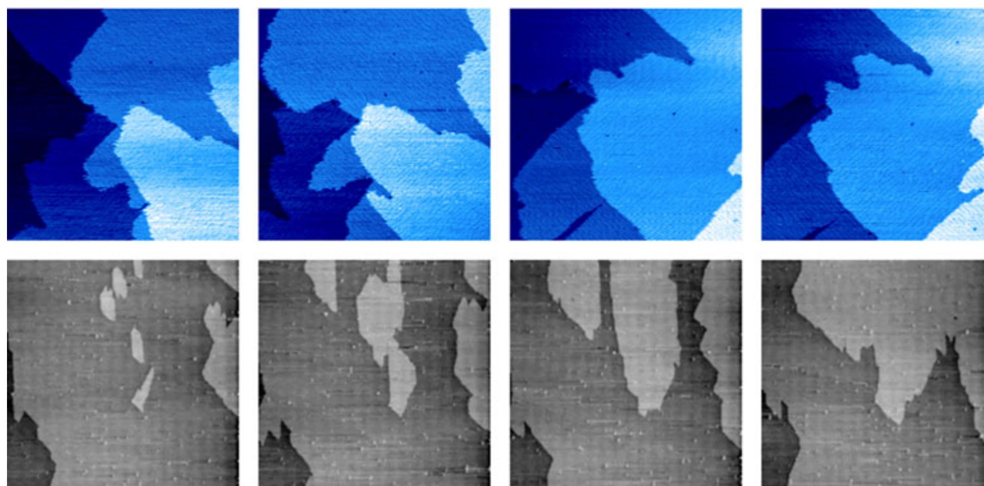

Figure 4. STM sequence (each image is recorded every 10 min) extracted from movies showing the homoepitaxy of Si. The growth rate is 3×10^{-4} ML s^{-1}: upper sequence Si(001) surface, (240×240) nm^2; lower sequence Si(111) surface, (2000×2000) nm^2.

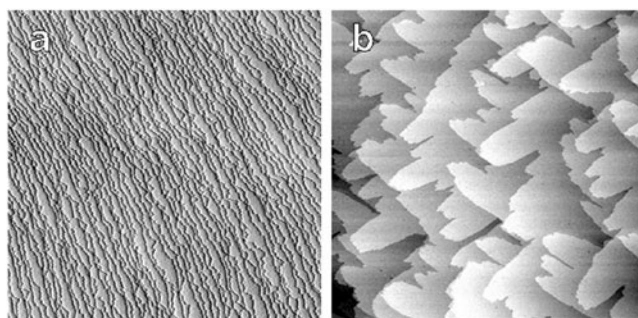

Figure 5. Homoepitaxy of Si on Si(001). STM images (3000×3000) nm^2 showing the epi-ready substrate (a), and the epi-layer surface (1000×1000) nm^2 after growth (b). In the latter case, the change from straight to zig-zag steps is evident.

distinguishable on the nanometric scale, are more appropriately discussed in terms of instability models. Theories of kinetic growth instability consider the presence on the surface of an array of steps. The microscopic approach considers, as a starting point, the adatoms on terraces where vacancies and kinked step edges are present. The processes controlling the evolution of steps in these models are adatom diffusion and the rate of attachment, detachment and incorporation at the step edge or at the step defect. Mesoscopic models, instead, consider that the diffusion and incorporation of the adatoms into the step is immediate, so the basic system is the step, with a continuous straight edge without kinks. Step evolution depends on the local terrace width, which leads to the step-bunching effect.

4.1. Naturally patterned surfaces

Ideal vicinal and high-index surfaces of proper orientation have a natural patterning made of regular arrays of steps and terraces. Step edges are preferred sites for attachment of surface diffusing adatoms; therefore, the natural patterning offers the possibility of guiding the

nucleation of the material added to the surface in compressively strained heteroepitaxy, leading, in principle, to the formation of ordered arrays of QDs. However, the practical use of 'natural' nanopatterned templates for controlling the self-aggregation process faces the difficulty of the initial regrowth of the homoepitaxial buffer layer on the stepped surface. In the majority of cases, kinetic instabilities come into play.

Burton, Cabrera and Frank (BCF) first introduced the concept of step-flow instability in the growth of vicinal orientations, leading to the bunching of an initially equally spaced train of steps [27]. In their original one-dimensional model, the main ingredient was the preferential incorporation of adatoms diffusing on terraces at the step edges, with different rates on the upper and lower side of the step [8]. Since then many other models have been developed which consider various non-equilibrium effects on the diffusion current in the presence of steps, leading to complex morphologies made of networks of bunched steps with fingerlike extensions (meandering) perpendicular to the initial straight edge [6, 7, 28–30].

As stated above, the key feature leading to step bunching and wandering is the asymmetry in the rate of attachment of adatoms at steps, by which they acquire a systematic drift perpendicular to the edge direction (uphill, downhill current). According to the different mechanisms [7, 8, 28] involved, the resulting current can either stabilize or destabilize the surface that consequently flattens or roughens. Several mechanisms embody the extra diffusion barrier for over-edge hopping at step edges, the Schwoebel barrier, which hinders the step-down of adatoms diffusing on top of a terrace. This fact, combined with preferential attachment to steps from the lower terrace, gives rise to instability of the surface.

4.2. Vicinal Si(001) surfaces and step bunching on the Si(111) surface

A simple way to obtain a natural nanopatterned substrate is offered by vicinal silicon surfaces. Si(001) substrates with different miscut angles can provide a natural method to control the rippled morphology of SiGe films grown on silicon [31, 32]. In figure 6 vicinal clean Si(001) surfaces are compared [33]. By changing the substrate miscut angle, it is possible to tune the ripple periodicity after Ge deposition.

A different mechanism occurs in the case of the Si(111) surface. On this surface, bunching of the regular array of steps [10] can be created by direct current heating. Several authors have studied this phenomenon [34–38] demonstrating that the final step configuration of the vicinal surface depends on the direction of flow of the heating current, on the miscut angle and on the temperature [34, 39, 40]. Temperature also has an effect [40]: for $T > 1220\,^{\circ}\mathrm{C}$ the bunching occurs in the step-down direction so that a regular array of bunched steps appears in the step-up direction. Both regular (R) and step bunched (SB) surfaces were obtained by flashing the sample with a current flow oriented in the step-up and step-down direction, respectively. In figure 7, we show an STM image of an R surface obtained by flashing in the step-up direction. It consists of a staircase of equally spaced fully reconstructed 7×7 bilayer steps, $\sim$65 nm wide and 0.31 nm high. From the image profiles the average miscut angle, $\theta < 0.3^{\circ}$, can be measured.

By heating in the step-down direction, an SB surface is obtained, as shown in figure 7(c) next to the line profile taken across the steps (figure 7(d)). In such a regime, terraces have an average width of 1350 nm and are separated by bunches about 8.5 nm high, corresponding to $N = 27$ atomic steps. From the measured staircase width $L_{\mathrm{b}} = 450$ nm, we derive the typical interstep spacing of the bunch, $l_{\mathrm{b}} = L_{\mathrm{b}}/N = 16.4$ nm, in good agreement with previous results [40]. The values measured are also in agreement with the BCF-like model of Stoyanov and Tonchev [41], which assumes a relation between the average step spacing l_{b} and the number N of steps in the bunch: $l_{\mathrm{b}} \propto N^{-2/3}$. So, by controlling some of the parameters such as the

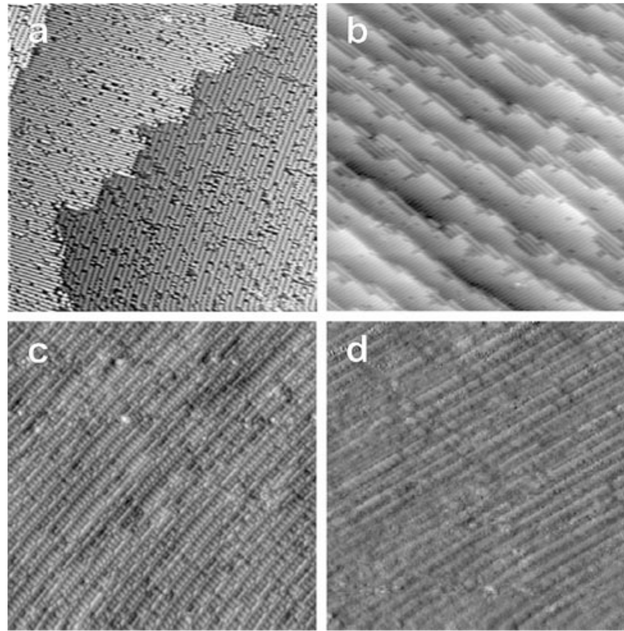

Figure 6. STM images of clean Si(001) surfaces: (a) singular surface (50×50) nm^2; (b) 2° vicinal surface (50×50) nm^2; (c) 8° vicinal surface (35×35) nm^2; (d) 10° vicinal surface (50×50) nm^2.

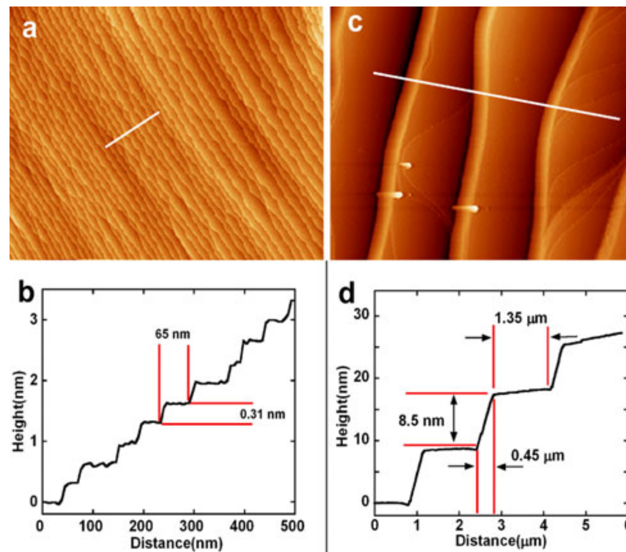

Figure 7. (a) STM topography $(2500 \times 1900 \times 10)$ nm^3 of an Si(111) R surface after flashing at $T = 1250\,^\circ$C with the current flowing in the step-up direction. (b) Height profile taken along the white line in (a). (c) STM topography $(7000 \times 5500 \times 36)$ nm^3 of an Si(111) SB surface after a flash at $T = 1250\,^\circ$C with current flowing in the step-down direction. (d) Height profile taken along the white line in (c).

current, the temperature and the miscut angle it is possible to obtain a different morphology and, in this way, a natural patterning of the surface [42].

5. Strain-driven instabilities in mismatched heteroepitaxy

'Heteroepitaxy' is the epitaxial growth realized by depositing an atomic species on a crystalline substrate of different composition. The forces acting between the substrate and the overlayer give rise to three types of macroscopic growth: layer-by-layer (Frank–Van der Merwe), 3D island formation on the bare substrate (Volmer–Weber) and a combination of the two, i.e. layer by layer up to a critical thickness and then island formation (Stranski–Krastanow).

From a thermodynamic point of view the three growth modes can be distinguished from the sign of $\Delta\gamma = \gamma_f + \gamma_{fs} - \gamma_s$. For the layer-by-layer growth $\Delta\gamma < 0$, because the surface formation energy γ_s is larger than that of the islands. Alternatively, if γ_s is smaller than $\gamma_f + \gamma_{fs}$, then $\Delta\gamma > 0$ and 3D clusters nucleate on the substrate. Such a growth mode is typical of *extremely large* lattice-mismatched systems, for example Ag on GaAs. If it happens that $\Delta\gamma$ is negative for the first few monolayers and then it changes sign at a critical thickness, the growth mode, called Stranski–Krastanow (S–K), changes from 2D to 3D. The latter is typical for the heteroepitaxy of *small and large* lattice-mismatched interfaces, like Ge on Si (4%) and InAs on GaAs (7%).

For S–K interfaces, many theoretical works have pointed out the existence of stress-induced instabilities in the strained overlayer below the critical thickness, in addition to the kinetic growth instabilities discussed in the previous section [43–47]. The isolated step of a highly compressed layer is unstable against undulation that allows for the release of elastic energy. For the train of steps on surfaces vicinal to singular orientations, the long-range interaction of the elastic distortions can introduce step bunching and/or step wandering. At large step distances, step wandering prevails, while at small distances step bunching dominates [47].

5.1. InAs/GaAs(001): the 2D phase.

5.1.1. Effect of the strain on the WL morphology. On unstrained real surfaces of singular orientation, like GaAs(001), the miscut steps initially present and the migration length of cations (of the order of few hundred nanometres) cause the rapid formation of new step fronts that, on standard growth conditions, lead to the jagged surfaces shown in figure 1. Typically, one recognizes three or four large terraces with meandered step edges and superimposed 2D islands forming, due to the Schwoebel barrier, more or less elongated mounds depending on the anisotropy of the surface diffusion.

The highly strained InAs/GaAs heteroepitaxy usually initiates on a GaAs substrate with the morphology of figure 1(a), since the buffer is grown at 590 °C, i.e. according to the kinetics of the (2 × 4) reconstructed (001) plane. Prior to InAs deposition, the temperature is lowered to 500 °C to minimize both In–Ga intermixing and In desorption [48]; therefore, the topmost GaAs plane changes its reconstruction from (2 × 4) to c(4 × 4).

For InAs thicknesses lower than 1.3–1.4 ML, an intermixed InGaAs WL forms, and the growth proceeds by step flow and nucleation of 2D islands [49, 50] at distances from step edges of the order of the cation migration length. At increasing depositions, coalescence of 2D islands gives rise to additional terraces and prevailing step-flow growth, as on vicinal surfaces. The meandering of step edges is enhanced with respect to that of the clean GaAs substrate (figure 8(a)), by partial relaxation of the accumulated strain energy. The long-range interaction of the elastic field starts the step-bunching process that increases from 0.7 to 1.6 ML of InAs deposition, as imaged in the AFM sequence of figures 8(b)–(d). At the highest coverage (figure 8(d)), the distance between steps in the bunch progressively decreases from ∼120 nm up to a minimum of 40 nm, regardless of the original substrate miscut.

One should notice that on these length scales, a few times the coherence length of RHEED, continuum theories fail, even for homoepitaxial growth. The predicted scaling of the surface

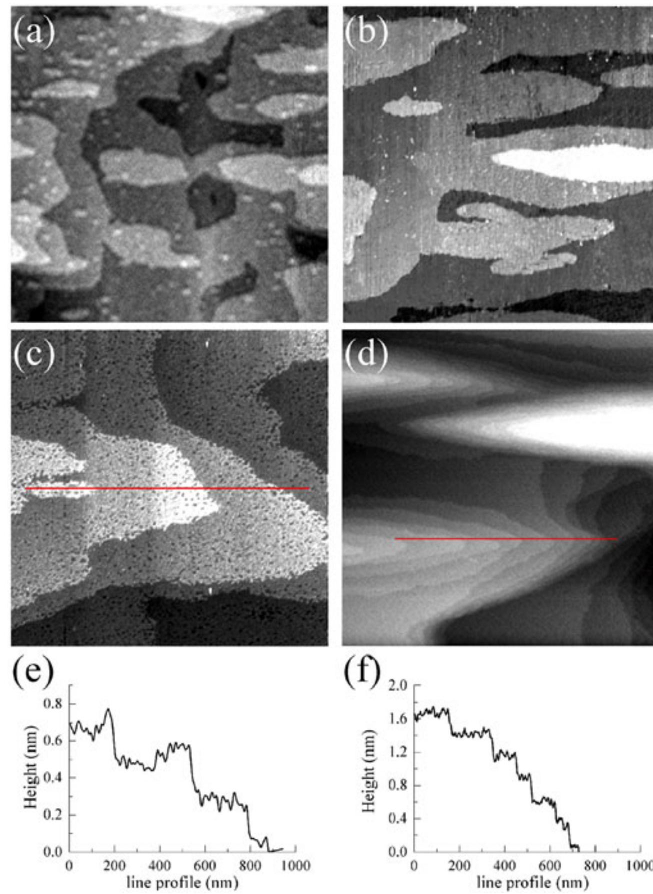

Figure 8. AFM topography, $1 \times 1\ \mu m^2$, of (a) 0.75 μm GaAs, (b) 0.7 ML InAs, (c) 0.9 ML InAs, (d) 1.1 ML InAs grown by MBE on GaAs(001). (e), (f) Height profiles along the lines marked in (c) and (d) respectively. Notice the progressive step bunching for increasing InAs depositions.

roughness with time (t^β) is in fact not consistent with the measured oscillatory behaviour of the RHEED intensity that monitors both symmetry and roughening of the growing surface. It should also be mentioned that the morphology, shown in figure 8, of a highly strained system does not contrast with those based on kinetic instability models, which do not explicitly include the strain.

To emphasize this point we show in figure 9 the topography of 1.3 ML of InAs on GaAs. The morphology of the $10 \times 10\ \mu m^2$ size image in figure 9(a) strongly resembles that of the clean GaAs surface of figure 1(a), while on the nanometre scale (figure 9(c)) step bunching appears. By exploiting the phase mode of the AFM, which evidences sharp variations of the profile, the topography of figure 9(a) transforms in to the 2D phase image of figure 9(b) that compares directly with figure 9(d) taken from [7], where the instability of a 2D step train is calculated based on a kinetic model.

Furthermore, the observation of a minimum distance (figures 8(d) and 9(c)) or, equivalently, of a steady-state velocity of the step train, agrees with models that exclude energetically costly overhangs and step crossing [7], or that attribute the step bunching to 'generalized impurities' that locally pin the propagating front [7, 29, 51].

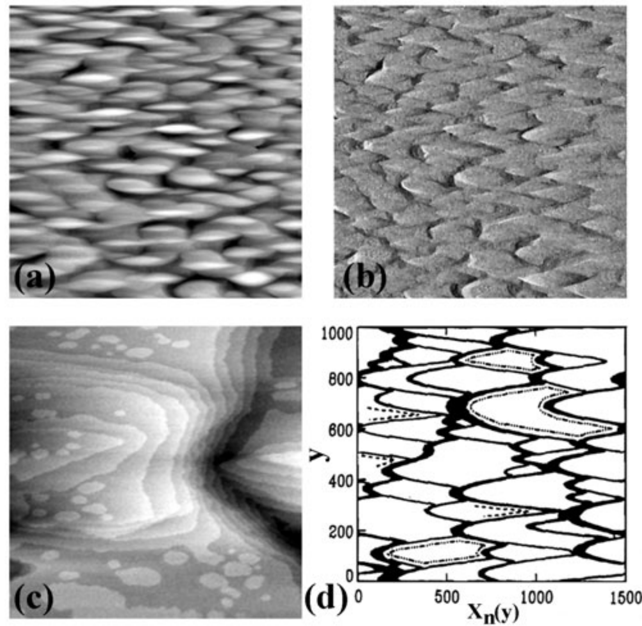

Figure 9. (a) AFM topography, $10 \times 10\ \mu m^2$, of about 1.3 ML of InAs deposited on the GaAs(001) substrate. Mounds, $1.2 \times 0.3\ \mu m^2$, about 3 nm high, are elongated in the $[1\bar{1}0]$ direction. (b) AFM 2D phase-image, $10 \times 10\ \mu m^2$, corresponding to topography (a) evidencing the sharp variations of the profile. (c) $1.5 \times 1.5\ \mu m^2$ image showing bunching of steps and nucleation of 2D islands on terraces. (d) Figure adapted from Kandel and Weeks [7] showing the numerical simulation of a step-train instability. Steps, moving from left to right, are marked by solid curves. Heavy solid curves correspond to step bunches.

5.1.2. WL atomic structure: intermixing and segregation. It is well established that the InAs epilayer is significantly alloyed with the GaAs substrate [3]. We show in figure 10 the atomically resolved STM topographies of the WL at 0.7 and 1.3 ML, and that of the $In_{0.2}Ga_{0.8}As$ alloy grown on GaAs(001) by MBE in the same experimental conditions as the WL. In figure 10(b) note the presence of zig-zag chains (bright strips) on the top surface for 1.3 ML coverage.

The formation of alloyed WL can be inferred by comparing its atomic structure with that of the alloy. Both the InAs WL and the In(Ga)As alloy surfaces displayed a dominant (1×3) LEED pattern and, only occasionally, faint traces of a (4×3) symmetry. The $\times 3$ translational symmetry of the top plane is the fingerprint for the In–Ga alloying [3]. Small domains of (4×3) and c(4×6) periodicity ($4\times$ along $[1\bar{1}0]$ and $3 \times (6\times)$ along [110] directions) are identified both on the WL at the two different thicknesses and on the alloy, as marked in panels (a), (b) and (c) respectively of figure 10.

More often, a (2×3) symmetry (with a weak correlation for the $2\times$ periodicity along the $[1\bar{1}0]$ direction) is found from RHEED and x-ray diffraction data on InGaAs alloys [52] and by STM measurements of the 2D growth of InAs on GaAs for depositions larger than 0.8 ML [3]. It should also be mentioned that a metastable (2×3) surface phase was observed after several hours annealing at 300 °C of the decapped GaAs(001) c(4×4) [53]. However, as pointed out by Zhang and Zunger [54], the (2×3) unit cell is not charge compensated and cannot be stable. As a matter of fact, high-resolution STM images [53] reveal that this symmetry consists of charge compensated (4×3) and c(4×6) domains, like those we detect on the WL and on the alloy

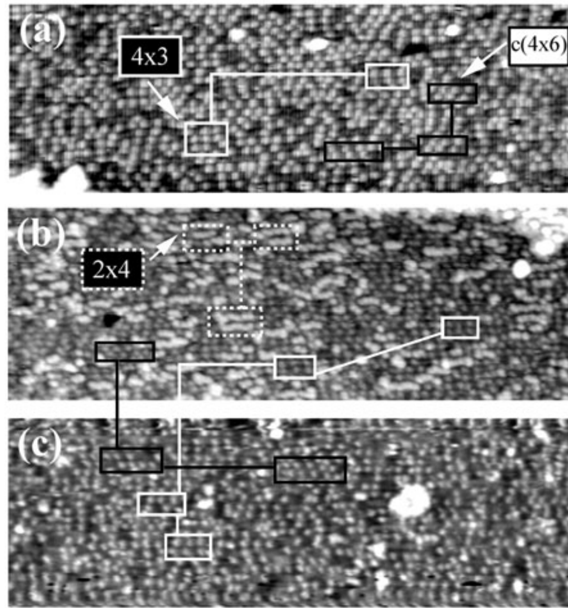

Figure 10. Atomically resolved, (30×90) nm^2, STM images of (a) InAs WL at 0.7 ML, (b) InAs WL at 1.3 ML and (c) $In_{0.2}Ga_{0.8}As$ alloy, 45 ML, grown by MBE on GaAs(001). Domains of (4×3) and $c(4 \times 6)$ periodicity are highlighted on the WL and the alloy. 2×4 InAs chains are detected only on the WL at 1.3 ML. The periodicity $(N \times M)$ is referred to the $[1\bar{1}0]$ and [110] directions, respectively, of the (001) surface cell ($a_0 \approx 4$ Å).

surfaces. The $\times 3$ (and $\times 6$) translational symmetry is generally maintained over large portions of the surface. The $4\times$ periodicity along $[1\bar{1}0]$ has a correlation limited to two or three unit cells and is hardly observed in LEED patterns, since the coherence area of the probe is much larger than the domain sizes. The reduced topological order is also in agreement with the suggestion of [55] for the existence of a 'liquid' surface layer with a certain degree of order caused by the lowering of the melting point at the high hydrostatic pressure induced by the strain.

Many experimental works in literature report on In segregation in epitaxial ternary III–V alloys. Among group III elements, In has the highest segregation coefficient, leading to the formation of a near-binary surface in ternary alloys. Moison *et al* [56] estimated, by x-ray photoemission and Auger measurements, an average surface In composition of 0.7 for the $In_{0.2}Ga_{0.8}As$ bulk compound, grown at 480 °C.

Dehaese, Wallart and Mollot (DWM) [57] have proposed a simple kinetic model to treat segregation processes far from equilibrium. At high flux and low growth temperature, in fact, the thermodynamic equilibrium model fails in predicting the concentration profiles. Because of the very low bulk diffusion coefficient at the typical temperatures for MBE growth, the DWM model rests on the hypothesis that the exchange between atoms A and B of a binary A_xB_{1-x} (ternary $A_xB_{1-x}C$) alloy can take place solely between the two topmost layers; namely, the growing layer, labelled with subscript 0, and the last layer of the substrate, or epilayer, labelled with subscript 1.

As far as the kinetic pathway is concerned, two rate quantities are considered: the probability per unit time, P_{10}, that atom A of the epilayer exchanges with atom B of the depositing layer, and the converse probability, P_{01}, that atom A from the depositing layer (0) exchanges with B of the epilayer (1). These two quantities, as usual, can be written as $P_{10} = \nu_{10}e^{-E_{10}/kT}$ and $P_{01} = \nu_{01}e^{-E_{01}/kT}$, ν_{10} (ν_{01}) being the attempt frequency of atom A for

the site exchange 1(0)–0(1) and E_{10} (E_{01}) the corresponding energy barrier. The evolution of the concentration of species A in the growing layer reads:

$$\dot{X}_0^{\mathrm{A}}(t) = F_{\mathrm{A}} + P_{10}X_1^{\mathrm{A}}(t)X_0^{\mathrm{B}}(t) - P_{01}X_0^{\mathrm{A}}(t)X_1^{\mathrm{B}}(t) \qquad (2)$$

where F_{A} (F_{B}), in ML s^{-1}, is the flux of atoms A (B) and $X_{0,1}(t)$ are time-dependent quantities expressed in fractions of a monolayer. Besides equation (2), two mass conservation laws hold, namely:

$$X_0^{\mathrm{A}}(t) + X_1^{\mathrm{A}}(t) = X_1^{\mathrm{A}}(0) + F_{\mathrm{A}}t \qquad (3)$$

and

$$X_0^{\mathrm{B}}(t) + X_1^{\mathrm{B}}(t) = X_1^{\mathrm{B}}(0) + F_{\mathrm{B}}t. \qquad (4)$$

Since $X_1^{\mathrm{A}}(t) + X_1^{\mathrm{B}}(t) = X_1^{\mathrm{A}}(0) + X_1^{\mathrm{B}}(0) = 1$, from equations (3) and (4) one gets

$$X_0^{\mathrm{A}}(t) + X_0^{\mathrm{B}}(t) = Ft, \qquad (5)$$

where $F = F_{\mathrm{A}} + F_{\mathrm{B}}$ is the total flux. By inserting equations (3) and (5) into (2) and changing to the independent variable $\theta = Ft$, one ends up with:

$$\frac{\mathrm{d}X_0^{\mathrm{A}}(\theta)}{\mathrm{d}\theta} = c_{\mathrm{A}} - [X_1^{\mathrm{A}}(0)(R_{10} - R_{01}) + R_{01}]X_0^{\mathrm{A}}(\theta) + (R_{10} - R_{01})[X_0^{\mathrm{A}}(\theta)]^2 - [c_{\mathrm{A}}(R_{10} - R_{01}) + R_{10}]\theta X_0^{\mathrm{A}}(\theta) + X_1^{\mathrm{A}}(0)R_{10}\theta + c_{\mathrm{A}}R_{10}\theta^2, \qquad (6)$$

where $c_{\mathrm{A}} = F_{\mathrm{A}}/F$, $R_i = P_i/F$ and $0 \leqslant \theta \leqslant 1$. Equation (6) can be easily solved numerically layer-by-layer, obtaining the composition profile of the alloy.

In applying equation (6) to the $\mathrm{In}_x\mathrm{Ga}_{1-x}\mathrm{As}$ alloy, the following parameters can be used [57]: $E_{10} = 1.8$ eV, $E_{01} = 2$ eV, $\nu_{10} = \nu_{01} = 10^{13}\ \mathrm{s}^{-1}$.

Recently, it was proposed by Walther *et al* [58] that the segregation of In to the surface of the WL in the growth of the $\mathrm{In}_x\mathrm{Ga}_{1-x}\mathrm{As}$/GaAs interface (with $x \geqslant 0.25$) controls the critical thickness of the 2D–3D transition. Using the DWM model [57] they derive a saturation value $x \simeq 0.85$ of the surface In composition at which strain is released by islanding.

By applying the same model, we calculated the In content of the surface and underlying layers in the cases of 45 ML of $\mathrm{In}_{0.2}\mathrm{Ga}_{0.8}\mathrm{As}$ and 1 and 2 ML of InAs on GaAs. On going from the top surface toward the bulk, the following values are obtained for the consecutive layers involved in the segregation process: (i) 0.83 for the top layer of the alloy; (ii) 0.82 (top layer) and 0.18 (second layer) for 1 ML of InAs on GaAs; (iii) 0.99 (top layer), 0.83 (second layer) and 0.18 (third layer) for 2 ML of InAs on GaAs. We remark that the same In fraction, close to the critical value 0.85 [58], is predicted in the former two cases, on account of the same atomic structure detected on the surface layer of the alloy, on the subsurface (second layer) of the WL at 1.3 ML and on surface domains for less than 1 ML coverage (0.7 ML in figure 10(a)).

An important difference exists between the alloy and the WL above 1 ML, i.e. the presence on the latter of zig-zag chains, one atomic plane ($a_0/4 \sim 0.14$ nm) above the subsurface, with (2×4) periodicity, out of tune with that of the substrate. One can speculate that, above 1 ML, the deposited In atoms form strained chains, that are mainly of InAs, ‘floating’ on top of the intermixed substrate [59]. This is consistent with the segregation model that anticipates an In surface fraction of 0.99 on completion of the second monolayer of InAs, and with the fact that the $\mathrm{In}_{0.82}\mathrm{Ga}_{0.18}\mathrm{As}$ alloyed surface formed on 1 ML deposition is that with the minimum Gibbs free energy [55]. This model for the WL has important implications for the 2D–3D transition at $\sim$1.6 ML, since an amount of loosely bound In, of the order 0.5–0.6 ML, is available at the surface which can participate in the surface mass transport responsible for the sudden volume increase of the 3D QDs, as will be discussed in section 6.1.

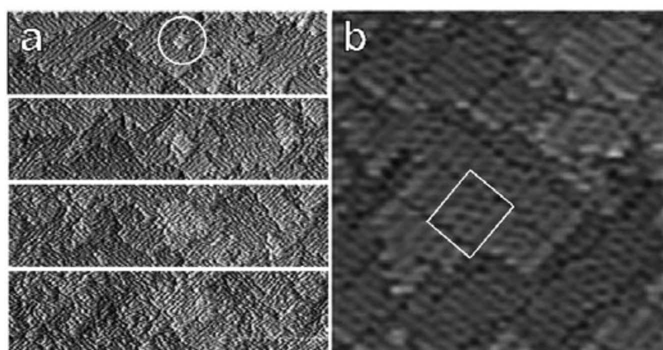

Figure 11. (a) STM images $(260 \times 95 \times 3)$ nm^3 acquired during the deposition of Ge at 550 °C presenting the WL formation. In the top panel different planes with dark rows corresponding to dimer vacancy lines are present. The mean distance between them is consistent with a $(2 \times N)$ reconstruction. During deposition these regions (see circle) enlarge to form a rough $(M \times N)$ reconstructed surface. (b) STM image $(155 \times 155 \times 3)$ nm^3 after 3 ML of Ge on Si(001). The WL at room temperature shows the coexistence of different reconstructions, e.g. the $c(4 \times 2)$ in the marked area.

5.2. Si–Ge/Si: the 2D phase

Ge/Si can be considered a model system of small mismatch (4%), because both species belong to the IV group and the bond is fully covalent. Therefore, the enthalpy at the Ge–Si interface depends essentially on the elastic energy connected to the bond deformation, and the calculation is particularly simple. However, the mixing of the two species is greatly favoured, mostly at high temperature, and the evaluation of the free energy requires much more complex calculations. The intermixing is also a serious limitation to the growth of small-sized QDs, because the real lattice mismatch is lower than expected and is the origin of large islands.

5.2.1. WL on Si(001) substrate. For a submonolayer coverage, the strain induced [60] by Ge deposition gradually transforms the Si(001)(2×1) surface reconstruction to $(2 \times N)$. The process consists of removing dimers on different rows forming a dimer vacancy line. As a function of the periodicity, N, between two dimer vacancy lines, the reconstruction is called $(2 \times N)$. By this mechanism, the surface reaches the first stage of strain relaxation. The periodicity of dimer vacancy lines decreases with Ge coverage down to a (2×8) reconstruction at 1 ML coverage, which is the configuration corresponding to the minimum surface energy. Theoretical calculations [26, 61] associate this reconstruction with an intermixing of 12% between Ge and Si. At higher coverages, between 2 and 3 ML, a second stage of strain relaxation occurs through the introduction of a few dimer vacancies into the *same* row, thus changing the surface reconstruction to $(M \times N)$ (figure 11(a)). Consequently, small structures arise forming 2D islands that produce the increase in the roughness. At high temperature, $(2 \times N)$ and $(M \times N)$ domains are made by lines of (2×1) dimers with a specific periodicity. However, at room temperature, dimers usually rearrange forming two typical reconstructions: the $p(2 \times 2)$ and the $c(4 \times 2)$ (figure 11(b)). Due to the Ge incorporation, atoms of the single Si–Ge or Ge–Ge dimer have different heights; the Ge atom is higher in position [62, 63]. Now, considering two adjacent dimer rows, if their direction is parallel an in-phase structure is established with a local $p(2 \times 2)$ reconstruction; if not, the structure is out of phase and it gives rise to the $c(4 \times 2)$ reconstruction [64].

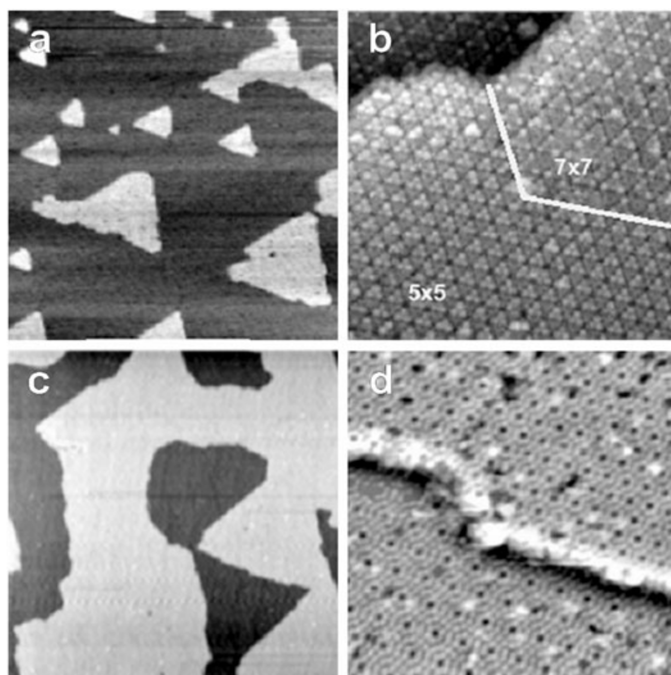

Figure 12. STM images of the evolution of the WL for increasing Ge coverage on Si(111). (a) Surface (260×260) nm^2 after 0.65 ML of Ge. (b) Surface (23.5×23.5) nm^2 after 1.35 ML of Ge. Note the mixed phase with the coexistence of two reconstructed domains (5×5) and (7×7). (c) Surface (260×260) nm^2 after 2 ML of Ge. (d) Zoom of the previous image (23.5×23.5) nm^2.

5.2.2. WL on Si(111) substrate. On Si(111), the growth of the WL proceeds up to a coverage of 3 ML (figure 12) as in the case of Ge/Si(001). Its evolution is well studied [65]: 2D islands form, presenting mixed (7×7) and (5×5) phases, and evolve maintaining the triangular shape induced by the symmetry of the silicon surface underneath. Increasing Ge coverage, these islands enlarge their size up to the formation of a complete flat layer, fully (5×5) reconstructed. The WL composition resulting from the intermixing and interdiffusion during the growth is evaluated by different experimental techniques, as STM [65], medium-energy ion scattering (MEIS) [66] and x-ray absorption fine structure (XAFS) [67]. An average composition of 50% is evaluated, although a precise determination of the occupation site of Si and Ge atoms is still lacking.

Regarding the growth mechanism: during the WL formation, a different evolution takes place depending not only on experimental parameters such as substrate temperature and growth rate, but also on the morphology of the substrate. The growth of the WL was filmed at a temperature of 400 °C, acquiring successive STM images on a selected area: at a Ge flux of 3.3×10^{-4} ML s^{-1} on a step-bunched surface with large terraces (figure 13(a)) and at higher flux, 2.5×10^{-3} ML s^{-1}, on a regular surface with small steps (figure 13(b)). In figure 13, four selected images of the movie illustrate the morphology obtained by the different growth mechanisms in the two cases. For a step-bunched substrate, on large terraces, 2D triangular islands nucleate and increase their size until the completion of the first flat layer. The second layer starts only when the first one is completed. In the case of the regular surface, the higher density of steps and the higher Ge flux produce the growth of more than one layer at a time. Layers evolve inducing the enlargement of the terrace width, as in the step-flow regime [68].

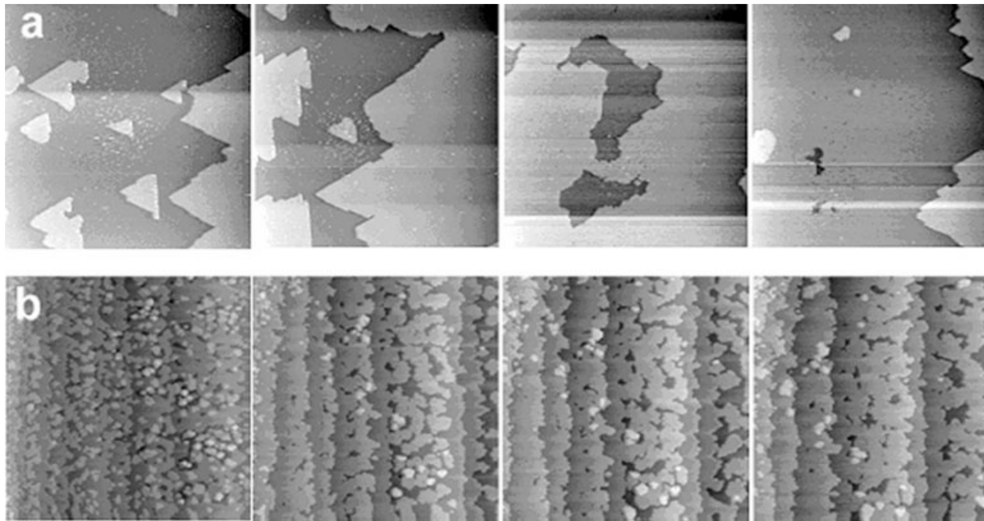

Figure 13. Ge/Si(111): growth of the WL at $T = 400\,^{\circ}$C: (a) $(0.3 \times 0.3)\ \mu\mathrm{m}^2$ STM images on a step-bunched surface with large terraces, low flux (3.3×10^{-4} ML min^{-1}); (b) $(1 \times 1)\ \mu\mathrm{m}^2$ STM images on a regular surface with small steps, higher flux (2.5×10^{-3} ML min^{-1}). Movies are available at www.fisica.uniroma2.it/infm/nanolab/.

6. Strain relaxation by QD formation

6.1. InAs/GaAs(001): 3D islands

Approaching the critical thickness, the surface morphology of the InAs/GaAs interface becomes quite complex. A typical morphology can be observed in the AFM image displayed in figure 14. The following features are worth noting: large and small 2D islands 1 ML high, small quasi-3D islands (quasi-3D QD) of height $\leqslant$2 nm and base size $<$20 nm, 3D QDs of height 3–4 nm and base-size $<$40 nm (labelled A, B, C respectively in figure 14). These features have been reported several times [69–73] but a definite conclusion on their role in QD nucleation has not yet been reached.

2D features like those labelled A in figure 14 contribute only to the final morphology and to the in-plane ordering of the QD array by supplying nucleation sites [16]. Figure 15 exemplifies the effect of step edges present on the surface in driving the alignment of 3D dots after the 2D–3D transition. Conversely, features B and C of figure 14 play an important role and require a more careful consideration.

Statistical data on the quasi-3D QDs and on 3D QDs acquired on an equal-sized area of the three samples shown in figure 16 are reported in the histograms and in table 1. We identify two clearly separated distributions for the quasi-3D QDs (400–1000 atoms) and the 3D QDs ($>$10 000 atoms) and the gap between them does not fill in at any InAs deposition. The quasi-3D QDs start nucleating between 1.4 and 1.5 ML of InAs, increase in number up to 1.7 ML and vanish above 1.9 ML, as also observed in [70]. Notably, the volume of the individual dots is decreasing monotonically, while their total volume remains negligible (see table 1). On the contrary, the height and basal area distributions of the 3D QDs between 1.5 and 1.9 ML narrow and shift to higher and lower values, respectively, while the single-dot volume becomes stationary. These observations are consistent with the existence of two equilibrium sizes for the 3D islands, one of which (quasi-3D QDs) is stable only for a limited range of InAs thicknesses, i.e. for a limited range of strain. The stable size of the 3D QDs has already

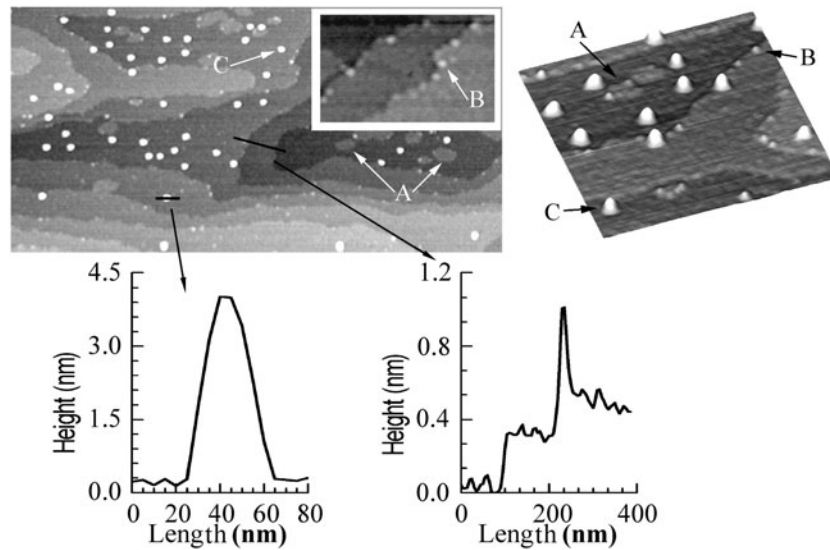

Figure 14. AFM topography, $(2 \times 1)\ \mu m^2$, of 1.5 ML of InAs on GaAs(001). The inset, $(400 \times 250)\ nm^2$, and the 3D image on the right, $(450 \times 450)\ nm^2$, evidence the nucleation of small 3D dots on the upper edge of the steps. The labelled features are: A, large and small 2D islands 1 ML high; B, small 3D dots (quasi-3D QDs) of height <2 nm and base size $\sim$20 nm; C, 3D quantum dots (3D QD) of height 3–4 nm and base size $\sim$40 nm. The height profiles of a 3D QD and of a quasi-3D QD nucleated at the upper edge of the step are shown.

Table 1. Mean values of the total volume, V, and of the number density, ρ, of quasi-3D QDs and the 3D QDs for the indicated InAs coverages, Θ. The volume of the single dot, $V_{\text{single dot}}$, is given in square brackets.

	V (ML) [$V_{\text{single dot}}$ (nm^{-3})]			ρ (10^{-4} nm^{-2})		
Θ (ML)	Quasi-3D	3D QD	Total	Quasi-3D	3D QD	Total
1.5	0.008 [130]	0.067 [1540]	0.075	0.22	0.15	0.37
1.7	0.006 [70]	0.670 [1070]	0.676	0.33	2.24	2.57
1.9	0.0006 [30]	1.459 [1040]	1.460	0.07	4.89	4.96

been discussed in the literature [74], and is related to a process of self-sizing induced by the balance between strain and bonding energy at the edge of the island. As shown in the inset of figure 14, small islands (labelled B) have the peculiarity of nucleating at the upper-step edge of 2D islands and terraces favoured by the strain relaxation and the step-down barrier (the Schwoebel barrier) for diffusing In adatoms [16]. Other works also report on small 3D islands, 2–4 ML high, detected in the same [73] or in different [69, 75] coverage ranges, but their distribution is not reported. In [71] a bimodal size-distribution of 3D QDs was found which gradually merged into a single one at increasing island density; however, this set of data is not directly comparable to the others or to ours by reason of the quite different experimental procedure used in growing the buffer layer and dots. Therefore, there is no real evidence that

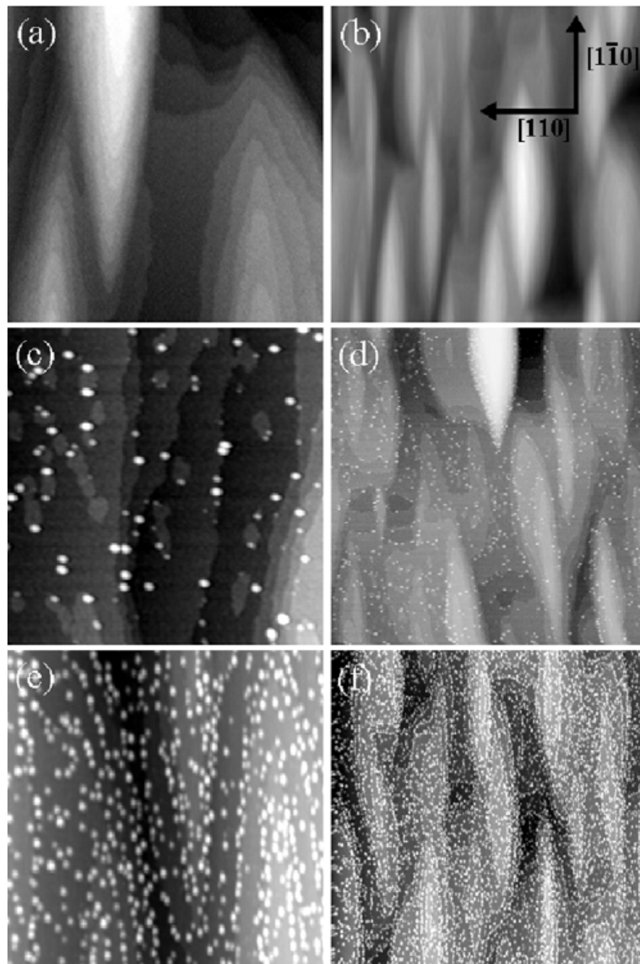

Figure 15. InAs QD arrays on GaAs(001). On the left, (800 × 800) nm^2 AFM images of 1.3 ML (a), 1.5 ML (c) and 1.7 ML (e) of InAs. On the right, are shown the corresponding large-scale images, (3 × 3) μm^2.

the nucleation of quasi-3D QDs is the first step of the self-assembly process and, in this sense, quasi-3D QDs do not seem to act as precursors of 3D QDs as we previously suggested [16] and other investigators affirm [69]. The evolution of the density and the volume of the 3D islands reported in table 1 supports the above consideration, since the low density and small volume involved in nucleation of the quasi-3D QDs cannot account for it.

At a coverage of 1.5 ML the total volume of dots is small. A large total volume variation of about 0.6 ML occurs at the 2D–3D transition between 1.5 and 1.7 ML (see table 1) because of the sudden nucleation of 3D QDs. At 1.9 ML the number density, ρ, of dots increases by a factor of 2 with respect to 1.7 ML, and by the same factor increases the total volume of 3D QDs due to the formation of equal-sized islands. The incoming atoms alone cannot explain these large volume variations. On going from 1.5 to 1.9 ML coverage, the total volume of dots changed by 1.38 ML: a fraction of this volume, 0.4 ML, is due to the incoming flux while the remainder, <1 ML, has to be accounted for by surface mass transport. If the model we propose for the WL is correct, approximately 0.5–0.6 ML of 'floating' In, loosely bound to the

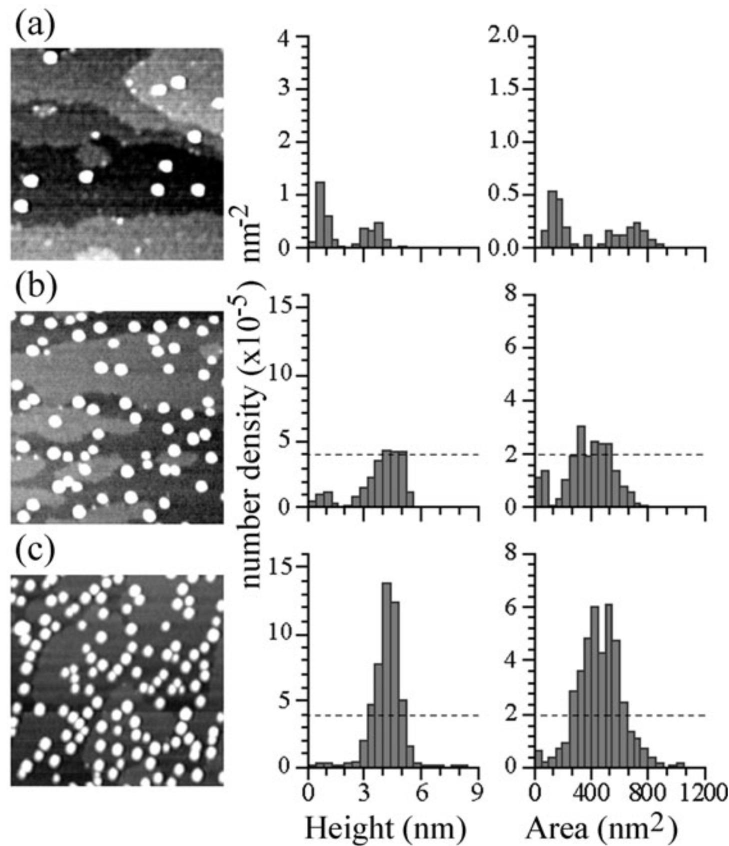

Figure 16. AFM images, (500 × 500) nm^2 of InAs dots on GaAs(001) at 1.5 ML (a), 1.7 ML (b), and 1.9 ML (c). On the right, the histograms of the height and basal area of the quasi-3D QDs and 3D QDs (labelled B and C in figure 14) are shown. The dashed lines help the comparison.

surface, will be available at the critical thickness for participating in the transition; i.e. more than 50% of that required to account for the nucleated volume of dots. There is still an amount of volume unaccounted for, but this is consistent with the experimental evidence that self-assembled InAs/GaAs QDs are themselves interdiffused [76] and participation of the substrate underneath and around islands must be invoked [77], as occurs for the Si–Ge system [67].

6.2. Si–Ge/Si: 3D islands

A great deal of work has recently been devoted to the study of the formation and the evolution of coherently strained 3D Ge islands on silicon surfaces [26, 78–84].

6.2.1. QDs on Si(001) substrate. On the Si(001) surface, the 2D–3D transition takes place at a coverage of 3–4 ML. On the WL, precursors, defined as *pre-pyramids*, form and evolve up to the full development of a {105} faceted pyramid. Stacked (2 × 1) Ge–Si layers pile up forming pre-pyramids that, in the case of $Si_{1-x}Ge_x$ alloys, have no definite facets. They increase the size up to the critical volume and after that a shape transition occurs with the formation of a regular pyramid [80]. In figure 17 the four reconstructed [85, 86] facets of a hut cluster are clearly shown. With increasing Ge coverage the pyramids grow, forming new planes on the facets, and finally undergo a morphological transition to dome-shaped islands [84].

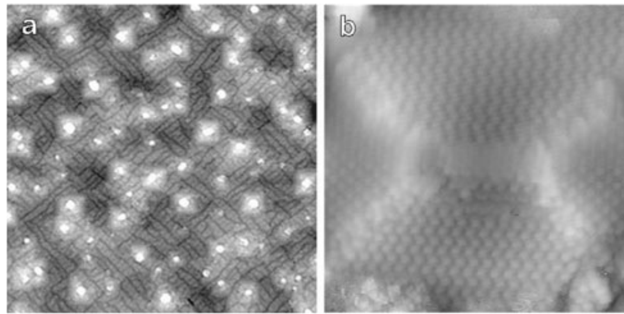

Figure 17. STM images of 3D Ge islands on Si(001). (a) (200×200) nm^2 view. Note the coexistence of 3D islands and WL regions where the reconstruction is still visible. (b) A single hut cluster (35×35) nm^2 bordered by $\{105\}$ facets.

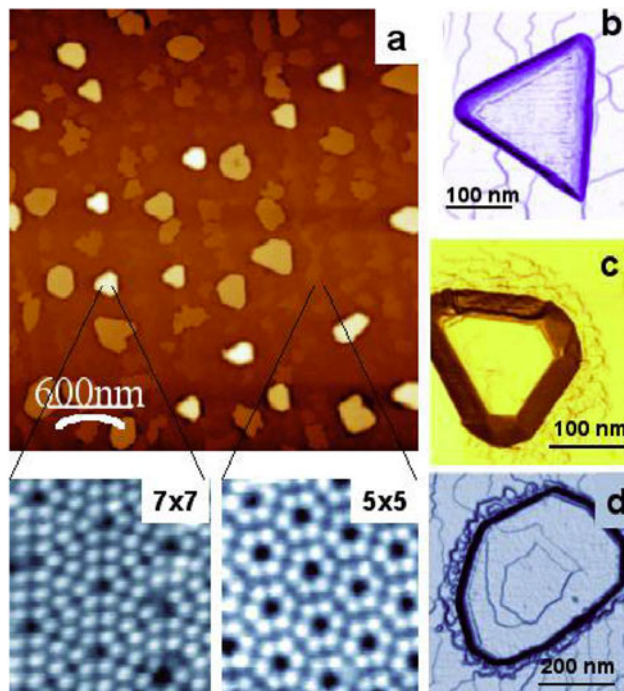

Figure 18. STM images of 3D Ge islands on Si(111). (a) A large view $(3000 \times 3000 \times 29)$ nm^3 of a regular surface after deposition of 17 ML of Ge at 500 °C. Note the zoom (8×8) nm^2 on top of the (7×7) reconstructed islands and on the (5×5) reconstructed WL. (b) A single triangular base island $(236 \times 236 \times 8.5)$ nm^3 at a coverage of 6.5 ML. (c) A Ge island $(230 \times 230 \times 40)$ nm^3 after 8 ML deposition, where new facets are inserted. (d) Ripened Ge island after deposition of 6.5 ML $(527 \times 527 \times 40)$ nm^3.

Tracking the epitaxial growth of this composite and intriguing system has provided very important information on the mechanism of growth [78, 79] and on the transition [80, 87] between different stages of its evolution.

6.2.2. QDs on Si(111) substrate. On Si(111), before the appearance of the three-dimensional Ge islands, a metastable strained state forms: the *supercritical* thick WL starts roughening and a depletion region develops caused by the material that migrates towards the steps [42, 88].

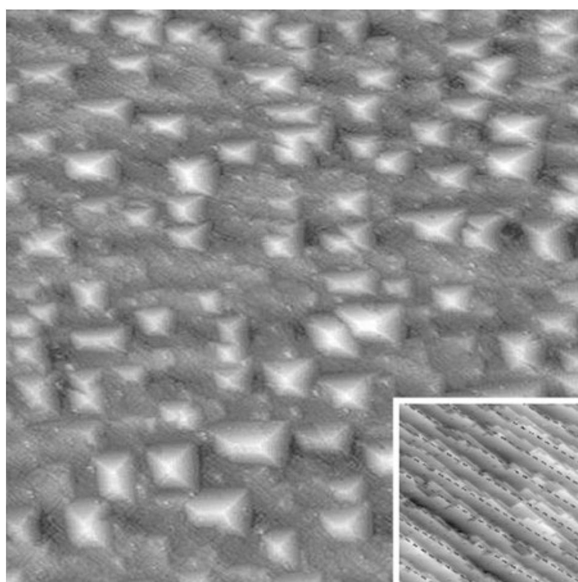

Figure 19. 3D Ge islands on Si(001) surface with a miscut angle of 2°; STM image (500 × 500) nm^2 after 9 ML coverage. The inset, (50 × 50) nm^2, shows the surface prior to deposition. Note the alignment of the 3D islands with respect to the step edges.

After that, 3D island nucleation takes place, starting at Ge coverage between 3 and 5 ML, depending on the Ge flux and on the substrate temperature [26, 82]. Figure 18 shows typical 3D islands where the (5 × 5) reconstruction of the WL and the (7 × 7) one of the top-plane of the islands are both visible. Initially, islands nucleate as truncated tetrahedra (figure 18(d)), with corners pointing in the $[11\bar{2}]$ direction. As reported in [83], this is due to the anisotropy of the growth rate in this direction. The (7 × 7) reconstruction of the top surface of the islands indicates substantial Ge–Si intermixing or, at least, the modification of the typical Ge(111) reconstruction caused by the stress field on the island [88]. We remark that the islands grow irrespective of substrate stepping and of the (111) orientation of the top facet.

In the next stage of island evolution, they become much higher and new steep facets develop. This shape transition (figure 18(c)) appears similar to that reported by Medeiros-Ribeiro *et al* [84] and Ross *et al* [89, 90], although in our case the area of the two kinds of islands does not change before and after the insertion of new facets. Notice the erosion of the substrate around the island.

Finally, the last step of island evolution is shown in the gradient image of figure 18(d). The shape is rounded, a central hole appears (0.6 nm deep) and a large amount of substrate around the island is eroded, as also observed on Ge/Si(001) [82]. The overall process can be qualitatively described as follows: the islands grow vertically up to a critical height, estimated to be about 48 nm [91], then the strain energy, stored inside the islands, can be partially relieved by introducing dislocations, or by a morphological transition of the islands that progressively round out their shape. A more extensive investigation of this topic is reported in [4].

6.2.3. Lateral ordering of Ge QDs. One example in which the morphological properties of the substrate can drive 3D island growth is provided by the Si(001) surface misoriented by 2°. In figure 19, the influence of the steps on the 3D island growth is evident: there is a lateral ordering of the island that is aligned parallel to the step edge (see the inset), which impedes the development of the hut on one side so that it assumes an asymmetric base.

To study the lateral ordering of Ge 3D islands grown on Si(111), we have followed the growth on the step-bunched surface shown in figure 20. After the completion of the WL,

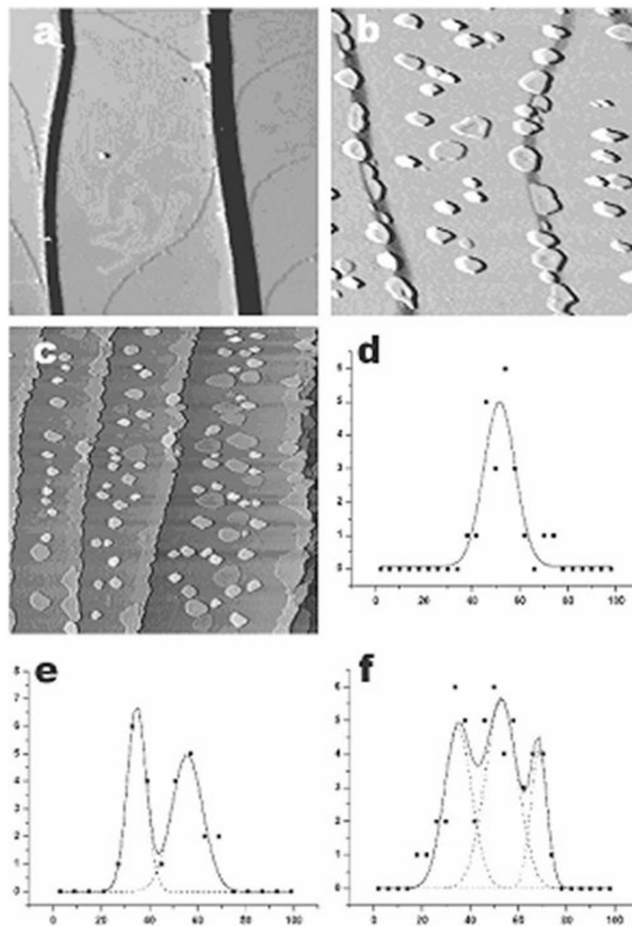

Figure 20. Distribution of 3D Ge islands on step bunched surfaces: (a) STM image ($7 \times 7 \times 0.025$) μm^3 of a step-bunched Si(111) surface; (b) after depostion of 9 ML of Ge; (c) the same surface ($10 \times 10 \times 0.035$) μm^3 after deposition of 19 ML of Ge. Normalized distributions of the relative island position for three ranges of width, w, of the terrace: (d) 1.2 μm $< w <$ 2.5 μm; (e) 2.5 μm $< w <$ 3 μm; (f) $w >$ 3 μm.

3D islands nucleate and evolve along step edges forming a continuous ribbon. When the process is completed, nucleation takes place at the centre of terraces and strongly depends on the terrace width. Figures 20(d)–(f) show the number of islands as a function of the ratio between their distance from the nearer upper step edge and the local width of the terrace. The island distributions have been plotted for three different ranges of terrace width. The result is apparent: a single row forms on the terraces ranging from 1.2 to 2.5 μm in width, while a double row forms on wider terraces (2.5 μm $\leqslant w \leqslant$ 3 μm). No definitive conclusion can be inferred for $w >$ 3 μm (figure 20(f)). Finally, STM images (not shown) reveal no islands on terraces as large as 1.2 μm [42].

6.3. Multistacked QD layers: role of the strain

On successive dot planes of multistacked QD structures (for instance, in a pile-up of InAs dot layers intercalated by GaAs spacers), the self-alignment of dots along the vertical (growth)

direction is obtained quite straightforwardly, because of the long-range interaction of the elastic strain–field coupling the different planes. This is an acquired result for technological applications.

The stress also couples the dots laterally (on the plane), giving, in principle, the possibility of obtaining an ordered lattice of QDs by a suitable engineering of the strain field. This possibility is at the basis of both 'natural' and 'artificial' methods of nanostructuring surfaces.

In heteroepitaxy, the strain is also a crucial parameter, besides temperature, to control the diffusion of adatoms during growth. The InAs/GaAs system can suitably exemplify this point.

InAs and GaAs have different lattice constants: 6.05 and 5.65 Å respectively. The $In_xGa_{1-x}As$ alloy has a lattice constant in between the two, given by the Vegard's law [92]. The InAs ($In_xGa_{1-x}As$) layer deposited on GaAs is compressively strained, and the GaAs layer is tensile strained if deposited on top of InAs ($In_xGa_{1-x}As$). Therefore, in the growth of multistacked QD structures, made up of InAs QD arrays intercalated by spacers of GaAs, diffusion of the In and Ga cations occurs alternatively on compressively and tensile strained interfaces. One could then expect large morphological changes on modelling the strain field in these structures.

For this system we observe by AFM quite different morphologies of the last InAs dot layer, depending on the thickness of the GaAs spacer in-between dot-layers.

Figures 21(b)–(d) show AFM images of the topmost InAs dot layer (2.7 ML) in three multistructures having GaAs(001)-c(4×4) spacers of 20 ML (c), 50 ML (d) and 100 ML (b). Figure 21(a), instead, is taken from Kamiya *et al* [93] and shows the AFM image of the GaAs capping layer, 18 ML, deposited on top of a single dot layer of InAs, of the same thickness and grown in the same conditions as our samples. For a single uncovered InAs dot array, dots are strained at the interface with the GaAs substrate and tend to relax at their top, assuming a lattice parameter close to that of the InAs bulk. Therefore, when the GaAs spacer is deposited on the InAs QDs, the higher misfit for GaAs is found on top of the large relaxed InAs dots. If the GaAs spacer is thin enough, volcano-like apertures appear corresponding to large relaxed InAs islands underneath, as seen in figure 21(a). As shown in figures 21(c) and (d), these apertures repeatedly form in the subsequent GaAs spacers even for a thickness of 50 ML. We remark that nucleation of InAs dots occurs solely into these apertures, signifying that the elastic field efficiently couples the successive dot layers.

Recent studies based on atomistic models employing first-principles total-energy calculations point out the effect of strain on the diffusion of group III cations on the GaAs(001) surface [94, 95]. In particular [94], the calculated diffusion barrier for In on the c(4×4) surface is a non-linear function of the surface misfit having a maximum for a compressive strain of about 3% and decreasing otherwise. Accordingly, we interpret our results considering that, due to the tendency of In to intermix and segregate on top of GaAs [56], the misfit of each InAs layer with the underlying GaAs spacer is reduced. This causes the lowering of the hopping barriers, an enhanced up-hill diffusion of In adatoms, and the nucleation of dots inside the volcano apertures, where the mismatch is at its smallest. However, when the thickness of the GaAs spacer is 100 ML (figure 21(b)), the tensile strain of the topmost layers of the spacer is fully relaxed. Hence, successive InAs layers are elastically decoupled and dot nucleation is similar to that of a single layer.

7. Artificial nanostructuring of surfaces

One of the crucial properties of samples produced for technological applications is the lateral ordering of the quantum structures. Very recently, several groups have presented new approaches for the growth of ordered patterns of homogeneous nanostructures. These

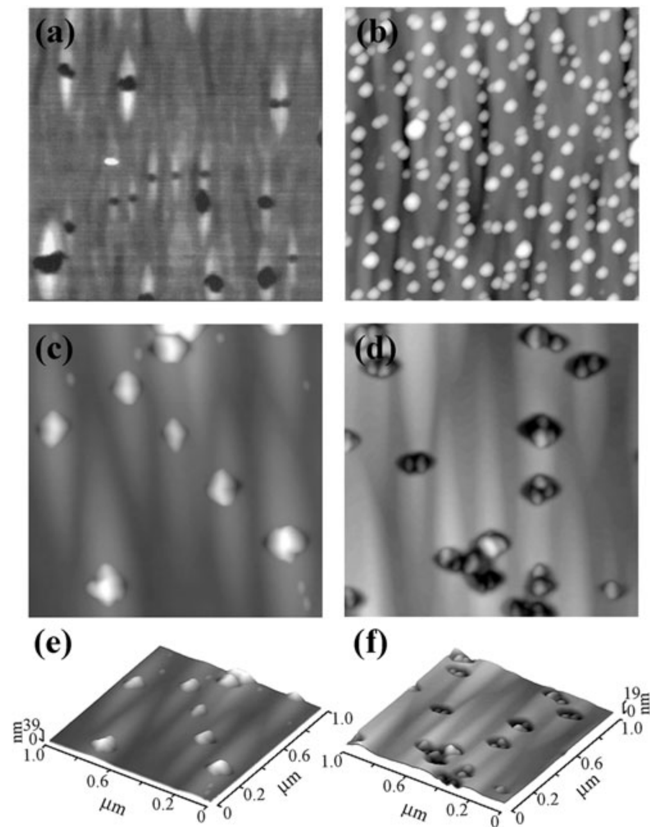

Figure 21. (a) AFM image, $1.0 \times 1.0\ \mu m^2$, adapted from Kamiya *et al* [93] showing the GaAs cap layer (18 ML) burying a single InAs dot layer (2.7 ML). Volcano-like apertures are seen on top of mounds elongated in the $[1\bar{1}0]$ direction. (b)–(d) $(1.0 \times 1.0)\ \mu m^2$ images of the topmost InAs layer (2.7 ML) of multistructures having GaAs spacers of thickness 20 ML (c), 50 ML (d), 100 ML (b). (e), (f) 3D plots of top views of (c) and (d), respectively.

include growth on mesa structures [96] or in SiO_2 windows [97, 98], patterning by surface instabilities [42, 99, 100] and nanolithography techniques such as nanoimprinting [101], EBL [102], implantation of Ga^+ ions [103] and *in situ* substrate patterning by STM or AFM [104, 105].

7.1. STM nanolithography

Arrays of pits or protrusions can be produced by an STM tip at selected locations on clean surfaces, constituting preferential sites for nucleation of QDs. This technique presents some advantages compared to nanostructuring by EBL or FIB. With the STM tip, it is possible to obtain *in situ* very small holes (of nanometre size) without changing the local surface composition, as may occur with the other methods that bring along contaminants like polymethylmethacrylate (PMMA) for EBL and Ga^+ for FIB.

Kohmoto *et al* [104] reported the first experiment where the STM approach was successfully applied to InAs/GaAs. The STM tip was used to leave metallic clusters at selected sites on the GaAs surface. The subsequent re-epitaxy of GaAs produced small holes in correspondence to the deposited clusters: these holes constitute the preferential nucleation sites

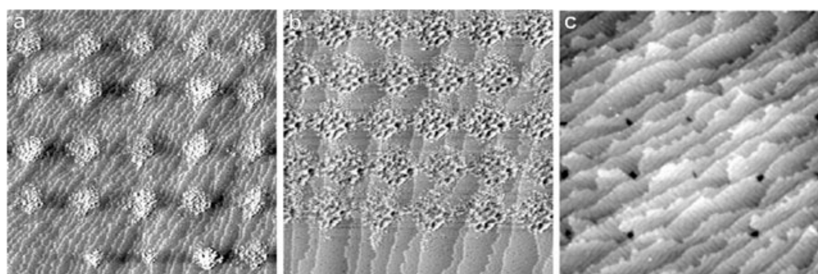

Figure 22. STM images of different STM lithography procedures: (a) after an I pulse, (900×900) nm^2; (b) after a V pulse, (500×500) nm^2; (c) after a Z pulse, (300×300) nm^2.

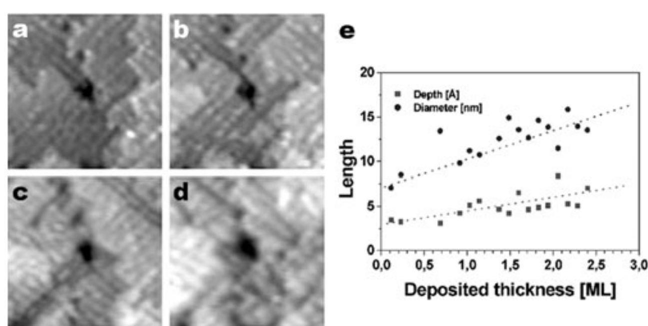

Figure 23. On-line growth of the WL on a nanostructured Si(001) surface. (a)–(d) Sequence of STM images $(50 \times 50 \times 0.5)$ nm^3 acquired during the Ge deposition at 550 °C for a coverage of (a) 0.89 ML, (b) 0.99 ML, (c) 1.24 ML, (d) 1.48 ML. (e) Evolution of diameter and depth of the hole as a function of the deposited thickness.

for the InAs dots. The method is very precise and clean, because the sample remains in UHV throughout the process. Nevertheless, it is not adequate for technological mass production, where large areas are required.

A similar method has been applied to obtain ordered arrays of Ge dots at specific locations on an Si(001) surface [105]. Different STM nanostructuring procedures have been tested: a current pulse, a voltage pulse or a Z pulse have been applied with the STM tip close to the surface (see figure 22). The best procedure found so far to achieve a regular array of ordered, small, clean holes consisted of applying a Z pulse by hitting the surface with the tip apex. Holes obtained by this way are stable and do not change their shape during annealing.

On samples nanostructured with different patterning parameters (pitches ranging from 100 down to 25 nm), the Ge deposition has been followed on-line by STM. Regarding the formation of the WL, one finds that Ge atoms do not fill holes, but on the contrary prefer to attach along the pit edge, forming a pseudomorphic layer that grows around the holes in step flow regime, as shown in figures 23(a)–(d). The evolution of the diameter and depth of the holes as a function of the deposited thickness, in figure 23(e), contains information about the growth mechanism.

By increasing the Ge deposition the transition from 2D pre-pyramids to hut clusters can be seen in figure 24. Initially, the pre-pyramids present a combination of two kind of structure: a few small $\{105\}$ protofacets and multiplane (2×1) reconstructed domains. When all of the partial $\{105\}$ domains are connected, the transition to the 3D pyramid is complete. Notice that the 3D islands form near the pits. The patterning of the substrate does not modify the

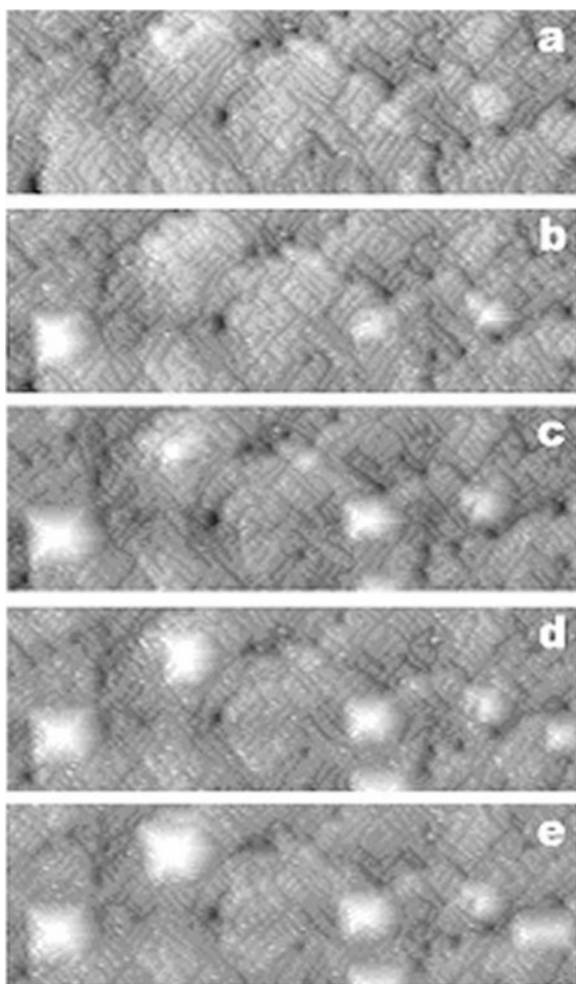

Figure 24. On-line growth of hut clusters on a nanostructured Si(001) surface. STM images $(250 \times 80 \times 3)$ nm^3 acquired during the deposition of Ge at 550 °C with a coverage of (a) 3.37 ML, (b) 3.51 ML, (c) 3.65 ML, (d) 3.79 ML, (e) 3.93 ML.

morphological properties of these hut clusters, such as faceting, reconstruction, dimension and shape. This result suggests that STM patterned surfaces could be suitable templates to induce lateral ordering [105].

7.2. Focused ion beam lithography

FIB system is similar to the scanning electron microscope, except that a beam of ions is used to scan across the sample. The ion beam is obtained from a liquid metal ion source (usually Ga). On one hand the interaction of the beam with the surface produces secondary electrons that provide the surface images; on the other, the ion beam can also be used for different processes, such as deposition or implantation of metal atoms, or etching of a specific area. The nanostructuring of semiconductor surfaces requires this last mode.

The ion beam is accelerated by a high voltage (4–150 KV) and displaced by a set of electrostatic lenses. With a spot size from 50 to 100 nm, the impact produces a hole. By increasing the voltage or repeating the procedure, holes of the desired depth are obtained. The realization of a motif can be achieved by means of software that controls the displacement of the beam. The FIB technique, therefore, allows for *in situ* high-resolution milling, as do other

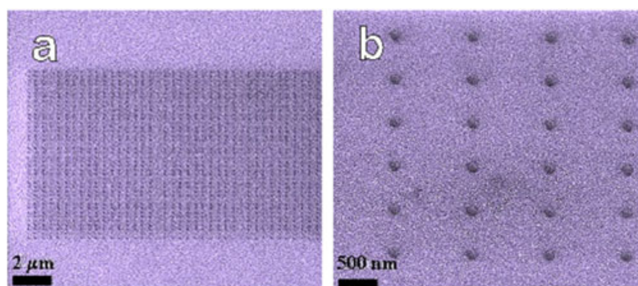

Figure 25. SEM images of an array of holes produced by a focused ion beam (FEI Company). Holes have a diameter of 100 nm, a depth of 10 nm and the distance between them is 1000 nm. (b) A detail of part of (a).

lithographic methods; however, possible Ga contamination cannot be excluded. This fact limits, at present, the wide applicability of the technique. Nonetheless, FIB technology is becoming an essential tool in semiconductor manufacturing [106]. For example, recent results suggest using FIB for the fabrication of single-electron memories.

An important field of application of the FIB technique is the production of 3D nanostructure arrays. By using Ga^+ heavy ions, it is possible to obtain direct etching of the Si surface at a scale of $<$10 nm. Figure 25 shows patterns of 40×40 holes (diameter 100 nm) with typical periodicity of 1000 nm. These samples were produced by the FEI Company (Eindhoven) on standard Si(001) wafers.

Regarding the growth of self-assembled Ge islands on these substrates, it was demonstrated recently that the nucleation is strongly dependent on the ion beam dose used for patterning [103, 106].

7.3. e-beam lithography

To predict the nucleation site of the dots, a new approach based on recent studies of Kawaguchi *et al* [107] using EBL appears very promising for the Ge–Si system. Holes in a Si substrate covered by a controlled oxide layer are produced by standard EBL, exposing the bare Si surface in selected regions where the Ge dots can nucleate and grow. It is well known, in fact, that Ge dots do not form on the oxide layer, so that only the clean Si surface allows for nucleation. A slight modification of this method makes use of *in situ* EBL to create holes, which should guarantee perfect cleaning and controlled growth conditions.

Ge growth on Si(001) covered by a 100 nm thermal oxide patterned by EBL has been studied. Samples are first cleaned by high-temperature annealing (1100 °C) in an H_2 atmosphere for several minutes and then overgrown with Ge using a CVD system. The results, reported in figure 26, shows that Ge islands can nucleate on the bare Si(001) substrate (left) while no islands are present on the flat oxide surface (right). So, the presence of SiO_2 allows control of the growth of the islands on samples patterned both by EBL [98] and by optical lithography [108].

The same procedure could be applied to obtain the selected nucleation of InAs QDs into microcavities produced by lithography and etching of a thin SiO_2 layer on GaAs. Figure 27 shows preliminary AFM results obtained by imaging a 10 nm thick SiO_2 layer deposited on epitaxial GaAs, before and after the growth of a 0.5 μm GaAs cap layer. While the oxide surface is quite flat, after the GaAs evaporation the surface is strongly roughened, suggesting that GaAs deposits on SiO_2 forming a coarse-grained amorphous film. A similar result is expected for

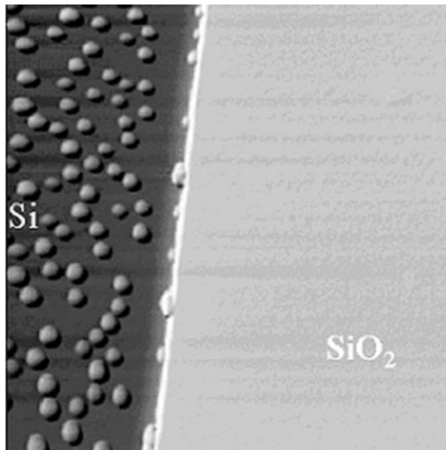

Figure 26. AFM image (5 × 5) μm^2 of Ge islands on a patterned SiO_2/Si(001) substrate grown by UHV–CVD.

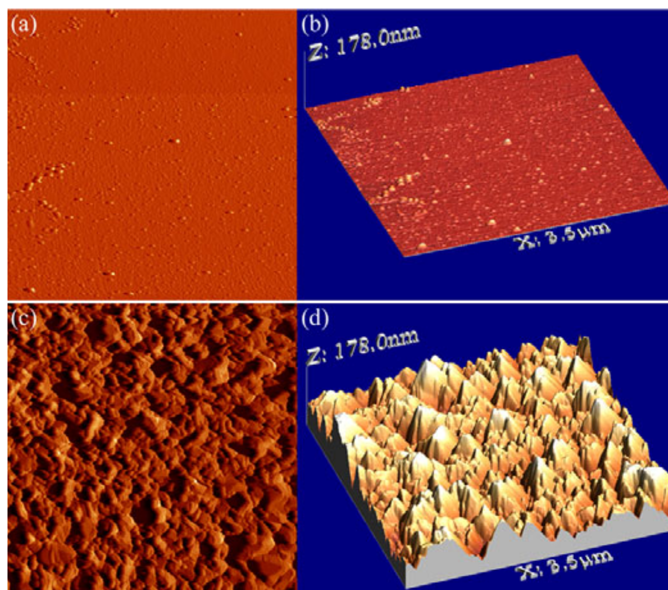

Figure 27. AFM top views, (3.5 × 3.5) μm^2, of: (a) 10 nm thick SiO_2 layer deposited on epitaxial GaAs(001) and (c) after evaporation of 0.5 μm of GaAs on top of the SiO_2 layer. (b), (d) 3D views of (a) and (c). The surface roughness of the SiO_2 is $\sigma = 0.30$ nm; after the GaAs deposition, it increases to $\sigma = 22$ nm.

InAs; QD nucleation could occur only on the GaAs substrate inside the microcavities where GaAs regrowth is epitaxial.

8. Concluding remarks

In order to characterize the morphology of group III–V and group IV–IV semiconductor surfaces, to be used as templates for the growth of ordered quantum nanostructures, the epitaxy of the prototype systems, InAs/GaAs(001), Si–Ge/Si(001) and Si–Ge/Si(111), which have quite different lattice mismatches, has been studied. It is shown how high-resolution

STM/AFM imaging at high temperature allows for the study of the fundamental processes of the homo- and heteroepitaxy of Si and Ge on Si(111) and Si(001) substrates. The influence of the surface reconstructions of the alloyed $In_xGa_{1-x}As$ phase has been studied by finding compelling evidence of the formation of In segregation at the $In_xGa_{1-x}As/GaAs$ interface. A quantitative calculation of the segregation process far from equilibrium predicts the composition profile versus InAs coverage of the few uppermost layers involved in the segregation process: 0.83 for the top layer of the alloy; 0.82 (top layer) and 0.18 (second layer) for 1 ML of InAs on GaAs; 0.99 (top layer), 0.83 (second layer) and 0.18 (third layer) for 2 ML of InAs on GaAs. This result is crucial to obtaining a detailed knowledge of the mechanism of formation of QDs at the critical thickness and to account for the observed nucleated volume of dots. The evolution of size in InAs/GaAs and shape of QDs in Si/Ge has been studied as a function of thickness: crossing the faceting transition, the characteristic shape modification from pre-pyramids to regular pyramids to domes has been thoroughly documented in both Si(001) and Si(111) surfaces. Lateral ordering of dots can be accomplished only with limited efficiency in both III–V and IV–IV systems if one relies on the natural morphology of the surface, but becomes a very promising issue if nanolithographic methods of nanopattering are adopted. We illustrate on Ge/Si the peculiarity of the recently suggested technique of STM nanopatterning in comparison with e-beam and FIB lithography: curiously one finds that Ge atoms do not fill pre-patterned holes on the substrate, but, on the contrary, atoms prefer to attach to the pit edge, forming a pseudomorphic layer that grows around the holes in the step-flow regime.

Acknowledgments

This work was supported by the Istituto Nazionale per la Fisica della Materia (INFM), by the Italian project COFIN 2002 and by the European Community FORUM-FIB contract IST-2000-29573.

References

[1] Horikoshi Y and Kawashima M 1989 *J. Cryst. Growth* **95** 17
Horikoshi Y 1994 *Handbook of Crystal Growth* vol 3b *Thin Films and Epitaxy* ed D T J Hurle (Amsterdam: North-Holland) p 691
[2] Balzarotti A, Fanfoni M, Patella F, Arciprete F, Placidi E, Onida G and Del Sole R 2003 *Surf. Sci. Lett.* **524** L71
Balzarotti A, Placidi E, Arciprete F, Fanfoni M and Patella F 2003 *Phys. Rev.* B **67** 115332
[3] Belk J G, McConville C F, Sudijono J L, Jones T S and Joyce B A 1997 *Surf. Sci.* **387** 213
[4] Motta N 2002 *J. Phys.: Condens. Matter* **14** 8353
[5] Shu D J, Liu F and Gong X G 2001 *Phys. Rev.* B **64** 245410
[6] Frank F C 1958 *Growth and Perfection of Crystals* ed R Doremus, B Roberts and D Turnbull (New York: Wiley) p 511
[7] Kandel D and Weeks J D 1994 *Phys. Rev.* B **49** 5554
[8] Schwoebel R L and Shipsey E J 1966 *J. Appl. Phys.* **37** 3682
Schwoebel R L 1969 *J. Appl. Phys.* **40** 614
[9] Duport C, Nozières P and Villain J 1995 *Phys. Rev. Lett.* **74** 134
[10] Latyshev A V, Aseev A L, Krasilnicov A B and Stenin S I 1989 *Surf. Sci.* **213** 157
Latyshev A V, Aseev A L, Krasilnicov A B and Stenin S I 1990 *Surf. Sci.* **227** 24
[11] Politi P, Grenet G, Marty A, Ponchet A and Villain J 2000 *Phys. Rep.* **324** 271
[12] Barabasi A L and Stanley H E 1995 *Fractal Concepts in Surface Growth* (Cambridge: Cambridge University Press)
[13] Krug J 1997 *Adv. Phys.* **46** 139
[14] Halpin-Healty T J and Zhang Y C 1995 *Phys. Rep.* **254** 215

[15] Kardar M, Parisi G and Zhang Y C 1986 *Phys. Rev. Lett.* **56** 889
[16] Patella F, Arciprete F, Placidi E, Nufris S, Fanfoni M, Sgarlata A, Schiumarini D and Balzarotti A 2002 *Appl. Phys. Lett.* **81** 2270
[17] Orme C, Johnson M D, Sudijono J L, Leung K T and Orr B G 1994 *Appl. Phys. Lett.* **64** 860
[18] Ballestad A, Ruck B J, Adamcyk M, Pinnington T and Tiedje T 2001 *Phys. Rev. Lett.* **86** 2377
[19] Rost M, Smilauer P and Krug J 1996 *Surf. Sci.* **369** 393
[20] Johnson M D, Orme C, Hunt A W, Graff D, Sudijono J L, Sander L M and Orr B G 1994 *Phys. Rev. Lett.* **72** 116
[21] Tejedor P, Allegretti F E, Smilauer P and Joyce B A 1998 *Surf. Sci.* **407** 82
[22] Chadi D J 1987 *Phys. Rev. Lett.* **59** 1691
[23] Takayanagi K, Tanishiro Y, Takahashi M and Takahashi S 1985 *J. Vac. Sci. Technol.* A **3** 1502
[24] Venables J A 1994 *Surf. Sci.* **300** 798
[25] Videcoq A, Pimpinelli A and Vladimirova M 2001 *Appl. Surf. Sci.* **177** 213
[26] Voigtländer B 2001 *Surf. Sci. Rep.* **43** 127
[27] Barton W K, Cabrera N and Frank F C 1951 *Phil. Trans. R. Soc.* A **243** 299
[28] Bales G S and Zangwill A 1990 *Phys. Rev.* B **41** 5500
[29] Kandel D and Weeks J D 1994 *Phys. Rev. Lett.* **72** 1678
[30] Krug J, Plischke M and Siegert M 1993 *Phys. Rev. Lett.* **70** 3271
[31] Teichert C 2002 *Phys. Rep.* **365** 335
[32] Berbezier I, Ronda A and Portavoce A 2002 *J. Phys.: Condens. Matter* **14** 8283
[33] Szkutnik P D, Ronda A, Sgarlata A, Balzarotti A and Motta N 2003 at press
[34] Yagi K, Minoda H and Degawa M 2001 *Surf. Sci. Rep.* **43** 45
[35] Jeong H C and Williams E D 1999 *Surf. Sci. Rep.* **34** 171
Metois J J and Stoyanov S 1999 *Surf. Sci.* **440** 407
[36] Metois J J, Heyraud J C and Pimpinelli A 1999 *Surf. Sci.* **420** 250
[37] Metois J J and Stoyanov S 1999 *Surf. Sci.* **440** 407
[38] Pimpinelli A, Videcoq A and Vladimirova M 2001 *Surf. Sci.* **175/176** 55
[39] Men F K, Liu F, Wang P J, Chen C H, Cheng D L, Lin J L and Himpsel F J 2002 *Phys. Rev. Lett.* **88** 096105
[40] Homma Y and Aizawa N 2000 *Phys. Rev.* B **62** 8323
[41] Stoyanov S and Tonchev V 1998 *Phys. Rev.* B **58** 1590
[42] Sgarlata A, Szkutnik P D, Balzarotti A, Motta N and Rosei F 2003 *Appl. Phys. Lett.* at press
[43] Tersoff J 1995 *Phys. Rev. Lett.* **74** 4962
[44] Tersoff J, Phang Y H, Zhang Z and Lagally M G 1995 *Phys. Rev. Lett.* **75** 2730
[45] Tersoff J and Pehlke E 1992 *Phys. Rev. Lett.* **68** 816
[46] Houchmandzadeh B and Misbah C 1995 *J. Physique* I **5** 685
[47] Léonard F and Tersoff J 2003 *Appl. Phys. Lett.* **83** 72
[48] Patella F, Nufris S, Arciprete F, Fanfoni M, Placidi E, Sgarlata A and Balzarotti A 2003 *Phys. Rev.* B **67** 205308
[49] Patella F, Fanfoni M, Arciprete F, Nufris S, Placidi E and Balzarotti A 2001 *Appl. Phys. Lett.* **78** 320
[50] Arciprete F, Balzarotti A, Fanfoni M, Motta N, Patella F and Sgarlata A 2001 *Recent Res. Dev. Vacuum Sci. Technol.* **3** 71
[51] Cabrera N and Vermilyea D A 1958 *Growth and Perfection of Crystals* ed R Doremus, B Roberts and D Turnbull (New York: Wiley) p 393
Eerden J P v d and Müller-Krumbhaar H 1986 *Phys. Rev. Lett.* **57** 2431
Croke E T, Grosse F, Vajo J J, Gyure M F, Floyd M and Smith D J 2000 *Appl. Phys. Lett.* **77** 1310
[52] See for instance, Sauvage-Simkin M, Garreau Y, Pinchaux R, Véron M B, Landesman J P and Nagle J 1995 *Phys. Rev. Lett.* **75** 3485
[53] Chizhov I, Lee G, Willis R F, Lubyshev D and Miller D L 1997 *Phys. Rev.* B **56** 1013
[54] Zhang S B and Zunger A 1996 *Phys. Rev.* B **53** 1343
[55] Bottomley D J 2000 *Japan. J. Appl. Phys.* **39** 4604 Part I and references therein
[56] Moison J M, Guille C, Houzay F, Barthe F and Van Rompay M 1989 *Phys. Rev.* B **40** 6149
[57] Dehaese O, Wallart X and Mollot F 1995 *Appl. Phys. Lett.* **66** 53
[58] Walther T, Cullis A G, Norris D J and Hopkinson M 2001 *Phys. Rev. Lett.* **86** 2381
Cullis A G, Norris D J, Migliorato M A and Hopkinson M 2002 *Phys. Rev.* B **66** 081305(R)
[59] Garcia J M, Silveira J P and Briones F 2000 *Appl. Phys. Lett.* **77** 320
Grandjean N, Massies J and Tottereau O 1997 *Phys. Rev.* B **55** R10189
Kaspi R R and Evans K 1995 *Appl. Phys. Lett.* **67** 819
Brandt O, Ploog K, Tapfer L, Hohenstein M, Bierwolf R and Phillipp F 1992 *Phys. Rev.* B **45** 8443
[60] Quin X R, Swartzentruber B S and Lagally M G 2000 *Phys. Rev. Lett.* **85** 3660

[61] Oviedo J, Bowler D R and Gillan M J 2002 *Surf. Sci.* **515** 483
[62] Bogusawki P and Bernholc J 2002 *Phys. Rev. Lett.* **88** 166101
[63] Li S D, Zhao Z G, Zhao X F, Wu H S and Jin Z H 2001 *Phys. Rev.* B **64** 195312
[64] Kahng S J, Park J Y and Kuk Y 1999 *Surf. Sci.* **440** 351
[65] Motta N, Sgarlata A, Calarco R, Nguyen Q, Castro Cal J, Patella F, Balzarotti A and De Crescenzi M 1998 *Surf. Sci.* **406** 254
[66] Sumitomo K, Kobayashi Y, Ito T and Ogino T 2000 *Thin Solid Films* **369** 112
[67] Motta N, Rosei F, Sgarlata A, Capellini G, Mobilio S and Boscherini F 2002 *Mater. Sci. Eng.* B **88** 264
[68] Motta N, Sgarlata A, Balzarotti A and Rosei F 2002 *Mater. Res. Soc. Symp. Proc.* **696** N2.2
[69] Krzyzewski T J, Joyce P B, Bell G R and Jones T S 2002 *Phys. Rev.* B **66** 121307(R)
[70] Ramachandran T R, Heitz R, Chen P and Madhukar A 1997 *Appl. Phys. Lett.* **70** 640
[71] da Silva M J, Quivy A A, Gonzalez-Borrero P P, Marega E Jr and Leite J R 2002 *J. Cryst. Growth* **241** 19
[72] Kobayashi N P, Ramachandran T R, Chen P and Madhukar A 1996 *Appl. Phys. Lett.* **68** 3299
[73] Heitz R, Ramachandran T R, Kalburge A, Xie Q, Mukhametzhanov I, Chen P and Madhukar A 1997 *Phys. Rev. Lett.* **78** 4071
[74] Barabasi A L 1997 *Appl. Phys. Lett.* **70** 2565
[75] Leonard D, Pond K and Petroff P M 1994 *Phys. Rev.* B **50** 11687
[76] Kegel I, Metzger T H, Lorke A, Peisl J, Stangl J, Bauer G, Garcia J M and Petroff P M 2000 *Phys. Rev. Lett.* **85** 1694
[77] Arciprete F, Patella F, Fanfoni M, Nufris S, Placidi E, Schiumarini D and Balzarotti A 2002 *Mater. Res. Soc. Symp. Proc.* **696** N6. 7.1
[78] Rastelli A and Von Känel H 2002 *Surf. Sci.* **515** L493
[79] Rastelli A and Von Känel H 2003 *Surf. Sci.* **532** 769
[80] Tersoff J, Spencer B S, Rastelli A and Von Känel H 2002 *Phys. Rev. Lett.* **89** 196104
[81] Vailionis A, Cho B, Glass G, Desjardins P, Cahill David G and Greene J E 2000 *Phys. Rev. Lett.* **85** 3672
[82] Voigtländer B and Zinner A 1993 *Appl. Phys. Lett.* **63** 3055
[83] Köhler U, Jusko O, Pietsch G, Muller B and Henzler M 1991 *Surf. Sci.* **248** 321
[84] Medeiros-Ribeiro G, Bratkovski A M, Kamins T I, Ohlberg D A and Williams R S 1998 *Science* **279** 353
[85] Raiteri P, Migas D B, Miglio L, Rastelli A and Von Känel H 2002 *Phys. Rev. Lett.* **88** 2561031
[86] Fujikawa Y, Akiyama K, Nagao T, Sukurai T, Lagally M, Hashimoto T, Morikawa Y and Terakura K 2002 *Phys. Rev. Lett.* **88** 176101
[87] Sutter P, Zahl P and Sutter E 2003 *Appl. Phys. Lett.* **82** 3454
[88] Seifert W, Carlsson N, Johansson J, Pistol M and Samuelson L 1977 *J. Cryst. Growth* **170** 39
[89] Ross F M, Tromp R M and Reuter M C 1999 *Science* **286** 193
[90] Ross F M, Tersoff J and Tromp R M 1998 *Phys. Rev. Lett.* **80** 984
[91] Capellini G, Motta N, Sgarlata A and Calarco R 1999 *Solid State Commun.* **112** 145
[92] Balzarotti A, Motta N, Kisiel A, Zimnal-Starnawska M, Czyzyk M T and Podgorny M 1985 *Phys. Rev.* B **31** 7526
[93] Kamiya I, Tanaka I and Sakaki H 1999 *J. Cryst. Growth* **201** 1146
[94] Penev E, Kratzer P and Scheffler M 2001 *Phys. Rev.* B **64** 085401
[95] Kley A, Ruggerone P and Scheffler M 1997 *Phys. Rev. Lett.* **79** 5278
[96] Jin G, Wan J, Luo Y H, Liu J L and Wang K L 2001 *J. Cryst. Growth* **227** 1100
[97] Nitta Y, Shibata M, Fujita K and Ichikawa M 2000 *Surf. Sci.* **462** L587
[98] Vescan L, Stoica T, Hollaender B, Nassiopoulou A, Olzierski A, Raptis I and Sutter E 2003 *Appl. Phys. Lett.* **82** 3517
[99] Motta N, Sgarlata A, Rosei F, Szkutnik P D, Nufris S, Scarselli M and Balzarotti A 2003 *Mater. Sci. Eng.* B **101** 77
[100] Ogino T, Homma Y, Kobayashi Y, Hibino H, Prabhakaran K, Sumitomo K, Omi H, Bottomely D, Kaneko A, Ling F, Zhang Z and Halsa M P 2002 *European MRS Meeting (Strasbourg, France, June 2002)* (Abstract S-VIII.1)
[101] Kamins T I, Ohlberg D A A, Stanley Williams R, Zhang W and Chou S Y 1999 *Appl. Phys. Lett.* **74** 1773
[102] Borgstrom M, Zela V and Seifert W 2003 *Nanotechnology* **14** 264
[103] Kammler M, Hull R, Reuter M C and Ross F M 2003 *Appl. Phys. Lett.* **82** 1093
[104] Kohmoto S, Makamura H, Ishikawa T and Asakawa K 1999 *Appl. Phys. Lett.* **75** 3488
[105] Szkutnik P D, Sgarlata A, Balzarotti A and Motta N 2003 *Mater. Sci. Eng.* C at press
[106] Hull R 2003 private communication
[107] Kawaguchi K, Usami N and Shiraki Y 2000 *Thin Solid Films* **369** 126
[108] Vescan L, Grimm K, Goryll M and Hollander B 2000 *Mater. Sci. Eng.* B **69/70** 324